Large-Scale Atmospheric Circulation Features of Warm and Cold Episodes in the Tropical Pacific

CLARA DESER* AND JOHN M. WALLACE

Department of Atmospheric Sciences, University of Washington, Seattle, Washington

(Manuscript received 30 May 1989, in final form 9 May 1990)

ABSTRACT

Ship observations of sea surface temperature (SST), sea level pressure and surface wind, and satellite measurements of outgoing longwave radiation (OLR) (an indicator of deep tropical convection) are used to describe the large-scale atmospheric circulation over the tropical Pacific during composite warm and cold episodes. Results are based on linear regression analysis between the circulation parameters and an index of SST in the tropical Pacific during the period 1946–85 (1974–89 for OLR). Warm episodes along the Peru coast (i.e., El Niño events) and basin-wide warmings associated with the Southern Oscillation are examined separately. Charts of the total as well as anomalous fields of SST, sea level pressure, surface wind and OLR for both warm and cold episodes are presented.

SST and surface wind anomalies associated with warm episodes are consistent with the results of Rasmusson and Carpenter (1982). El Niño events are characterized by strong positive SST anomalies along the coasts of Ecuador and Peru and along the equator eastward of 130°W, and by an equatorward expansion and intensification of the Inter Tropical Convergence Zone (ITCZ) over the eastern Pacific. Basin-wide warm episodes exhibit positive SST anomalies along the equator eastward of 170°E, a southward expansion and intensification of the ITCZ, and an eastward shift and strengthening of the Indonesian convective zone. The movements of the precipitation zones are in good agreement with anomalous large scale surface wind convergence. Meridional wind anomalies dominate the anomalous surface convergence throughout the tropical Pacific.

Surface winds are consistent with the sea level pressure distribution, with down-gradient flow near the equator, and with Ekman balance in the subtropics. A center of below normal sea level pressure over the equatorial eastern Pacific, distinct from the negative pressure anomalies over the subtropical southeast Pacific, is observed during basin-wide warm episodes. This equatorial feature is highly correlated with local SST and appears to be a boundary layer phenomenon.

There is a net increase in deep convection over the tropical Pacific during warm episodes. Enhanced convection in the ITCZ during warm years is not accompanied by a net increase in surface wind convergence. A comparison between precipitation and surface wind convergence suggests that moisture convergence extends through a deeper layer in the equatorial western Pacific than in the ITCZ over the eastern Pacific.

The contrasting distributions of surface relative humidity, total cloudiness, and air–sea temperature difference over the eastern tropical Pacific during basin-wide warm and cold episodes are described in the context of boundary layer processes.

1. Introduction

In a landmark paper, Rasmusson and Carpenter (1982) described the variations in sea surface temperature (SST) and surface wind over the tropical Pacific Ocean associated with a composite El Niño/Southern Oscillation (ENSO) warm episode. Their composite, based on six warm episodes along the coast of Peru, has become a standard of comparison for numerical model simulations of ENSO (c.f., Zebiak and Cane 1987). In their composite, strong positive SST anomalies are observed along the coasts of Ecuador and Peru and in the eastern equatorial Pacific around April–June. This coastal warming is followed by the appearance of weaker but spatially coherent positive SST anomalies extending across the entire equatorial Pacific eastward of 170°E. The basin-wide warming, which reaches maximum intensity late in the year, is accompanied by westerly surface wind anomalies in the equatorial western Pacific and anomalous northerly flow across the mean position of the Inter Tropical Convergence Zone (ITCZ). Rasmusson and Carpenter's study contained more limited information on surface pressure and rainfall anomalies associated with the composite warm episode. Their pressure analysis was restricted to islands in the southeast Pacific and Darwin, Australia; stations located near the centers of action of the Southern Oscillation. A negative swing of the Southern Oscillation, indicative of a weakening

* Present affiliation: Cooperative Institute for Research in Environmental Sciences, Campus box 216, University of Colorado, Boulder, CO 80309.

Corresponding author address: Dr. Clara Deser, CIRES, Campus Box 216, University of Colorado, Boulder, CO 80309-0216.

© 1990 American Meteorological Society

of the sea level pressure gradient across the tropical Pacific, accompanies the composite warm episode. Enhanced precipitation is observed at the Galapagos Islands during the time of peak coastal SST anomalies and pronounced positive rainfall anomalies are observed at islands in the equatorial western Pacific during the basin-wide warming. Rasmusson and Carpenter (hereafter referred to as RC) noted that these composite rainfall anomalies are comparable in magnitude to the anomalous large-scale vapor flux convergence.

The purpose of this paper is to extend the RC study to include additional meteorological parameters [sea level pressure, outgoing longwave radiation (a proxy for deep cumulus convection), sea–air temperature difference, relative humidity and cloud amount]; both their total and anomalous distributions. The sea level pressure field provides insight into how the low-level atmospheric circulation is forced by SST variations and provides a dynamical context for the surface wind changes. The distribution of atmospheric convection is an integral component of the circulation; its relationships to the SST and surface wind fields are crucial to understanding the ENSO phenomenon. The distributions of sea–air temperature difference, relative humidity, and cloud amount affect the surface energy balance and, as will be shown, shed light on atmospheric boundary layer processes.

Although most ENSO studies (including RC) emphasize anomalies, it is becoming increasingly apparent from modeling experiments that the mechanisms responsible for atmosphere/ocean interaction strongly depend upon the mean fields upon which the anomalies are superimposed. For example, the distribution of deep convection in the atmosphere appears to be more sensitive to changes in SST in regions of high SST (such as the western equatorial Pacific) than in regions of low SST (such as the eastern equatorial Pacific), and a surface wind anomaly of a given amplitude will cause a larger perturbation in surface wind stress (e.g., oceanic forcing) if it is superimposed upon a strong mean surface wind rather than a light one.

Our procedure for constructing warm episode composites was motivated by several recent developments in ENSO research. It is now widely recognized that the tropical Pacific undergoes pronounced cold periods that are just as coherent as their warm counterparts (Philander 1985, Wright et al. 1988, and Kiladis and van Loon 1988). Therefore, we describe cold episodes as well as warm episodes. Deser and Wallace (1987) have shown that warm episodes along the Peru coast and basin-wide equatorial Pacific warm episodes are not as tightly linked as one might infer from the RC composite. For example, the two warm episodes of the 1980's followed a different pattern from the RC composite with SST anomalies first appearing in the equatorial central Pacific and subsequently along the Peru coast. In addition, coastal warm episodes have occurred in the absence of basin-wide warmings and vice versa (Deser and Wallace 1987). The analysis technique used in this study discriminates between these two phenomena.

To address these issues, we have constructed composites for warm and cold years in which we are careful to distinguish between the warm episodes along the Peru coast [which correspond to El Niño events documented by Quinn et al. (1987) and Deser and Wallace (1987)], and the basin-wide warmings associated with the Southern Oscillation. Our composites include total as well as anomalous fields of SST, sea level pressure, surface wind and OLR over the tropical Pacific. We focus on the coherent simultaneous relationships among the four parameters during the seasons when the interannual variability is most clearly defined. For the coastal warmings, we examine the period March–May (the end of the climatological warm/rainy season in the eastern equatorial Pacific) that corresponds to the "Peak Phase" of the RC composite when SST and rainfall anomalies along the Peru coast are near their maximum. We use two seasons to represent the basin-wide warm episodes: July–November and December–February. The July–November season was emphasized by Wright et al. (1988) and marks the cold season in the eastern equatorial Pacific. December–February corresponds to the "Mature Phase" of the RC composite and is the season most often used for general circulation model simulations of ENSO. Our March–May warm episode composites are representative of coastal El Niño events regardless of whether they precede or develop separately from basin-wide warmings, and our July–November and December–February warm episode composites are representative of basin-wide warmings during the cold season irrespective of whether they are associated with coastal El Niño events.

A description of our data and analysis scheme follows in section 2. The composites of total and anomalous SST, sea level pressure, surface wind and OLR for coastal cold and warm episodes are presented in section 3; those for basin-wide warm and cold episodes are shown in section 4. Section 5 contains additional cold and warm episode composites of parameters relevant to the surface energy balance (air–sea temperature difference, relative humidity and cloud amount) for the July–November season. The results are discussed in section 6.

2. Data and analysis procedure

The SST, surface wind, sea level pressure, cloud amount, sea–air temperature difference and relative humidity data used in this study are from the Comprehensive Ocean-Atmosphere Data Set (COADS), the largest compilation of observations from ships-of-opportunity over the world oceans (see Fletcher et al. 1983). These data are in the form of monthly means for each 2° latitude/longitude square. We used obser-

vations from the period 1946–85. Satellite measurements of OLR were provided by the Climate Analysis Center in the form of monthly means for the period 1974–89 (excluding March–December 1978). Originally archived by 2.5° squares, the OLR data were interpolated onto a 2° latitude × 2° longitude grid for compatibility with the ship observations. We have also made use of Sadler et al.'s (1987) hand analysis of long-term monthly mean SST, sea level pressure, and surface wind fields from the COADS. These fields are based on data for the period 1900–79 and digitized onto a 2° latitude × 2° longitude grid over the tropical oceans.

In our previous work (Wright et al. 1988), we used linear regression analysis to define anomalous conditions associated with warm episodes. We justified this approach on the basis of the observed symmetry between warm and cold episodes. The major advantage of linear regression analysis over compositing is that the results contain more degrees of freedom. In the present study, we have constructed warm and cold composites from the linear regressions as follows. For the coastal warm episodes, March–May averages of the parameters in each 2° × 2° grid box over the tropical Pacific were regressed upon March–May averages of SST at Pt. Chicama (8°S) on the Peru coast, a widely used indicator of El Niño (see RC, Wyrtki 1975). As noted in the Introduction, the season March–May corresponds to the "peak phase" of the RC composite. Similarly, for the basin-wide warm episodes, July–November and December–February averages of the parameters were regressed upon July–November SST averaged over the equatorial Pacific [6°N–6°S, from the dateline to the South American coast, respectively]. This SST index is based on anomalies for each 2° square, weighted by the number of observations. The region used in computing the index corresponds to the primary center of action of the first nonseasonal EOF of SST in the tropical Pacific (Weare et al. 1976). The seasons July–November and December–February exhibit coherent basin-wide warm episode anomalies (RC, Wright et al. 1988). The regressions are based on the period 1946–85 (1974–89 for OLR); data for 1983 were excluded from the March–May composites because Pt. Chicama SST was more than 4 standard deviations above normal during that period. Maps were constructed of the resulting regression coefficients in each 2° square over the tropical Pacific Ocean. These regression maps may be regarded as typical anomaly fields associated with the coastal and basin-wide warm episodes (cold episodes if the signs are reversed). Only those features in the regression fields that are correlated at a level far above the 0.05 significance level on the basis of a 1-tailed Student's t test are emphasized in this study. Correlation coefficients with absolute values of 0.30, 0.41, and 0.45 correspond to the 0.05, 0.01, and 0.001 significance levels, respectively, for a time series 40 years in length [taking into account the 1-year autocorrelation of the SST indices during the period 1946–85 (~ -0.2)]. For the short OLR record, a correlation coefficient of 0.46 in absolute value is significant at the 0.05 level.

Time series of anomalous SST at Pt. Chicama on the Peru coast during March–May and the equatorial Pacific SST index during July–November and December–February are shown in Fig. 1. The six warm episodes composited by RC (1951, '53, '57, '65, '69, '72) are prominent in all three indices, with the exception of 1953 in the December–February index. Pronounced positive SST anomalies also occurred in March–May 1948, '58, '59, '83 and '87 at Pt. Chicama and in July–November and December–February 1963, '68, '76, '79, '82, '86 and '87 in the equatorial Pacific SST index. The cold episodes 1950, '54–55, '64, '70, '73 and '88 are common to all three indices. In addition, cold events occurred in March–May 1968 and '86 at Pt. Chicama and in July–November and December–February 1949, '67 and '75 in the equatorial Pacific SST index. The coastal and basin-wide regression fields are thus based on somewhat different linear combinations of the years.

By using linear regressions to derive anomalies characteristic of both warm and cold episodes, we have tacitly assumed that the two sets of anomalies are similar in structure but opposite in sign. There is substantial evidence in the literature to support this assumption [see Philander (1985), Meehl (1987), Kiladis and van Loon (1988) and Wright et al. (1988)]. As a check on this method of treating the data, we constructed composite anomaly fields for the 12 warmest and the 12 coldest years during the period 1946–85. The results (not shown) confirm that warm and cold composite anomalies exhibit similar spatial structures with opposite polarity; however, the anomalies in the warm composites are about 1.5 times stronger than those in the cold composites (Deser 1989).

In order to reconstruct the total fields for typical warm and cold episodes, anomaly fields based on the regression coefficients were added to and subtracted from climatology, respectively. Pazan and Meyers (1982) have used a similar approach to derive the total surface wind fields during positive and negative phases of the Southern Oscillation. The anomaly fields used in the warm episode reconstructions are the regression coefficients multiplied by the average SST anomaly index for the 5 warmest years on record (2.6°C for Pt. Chicama, 1.4°C for the July–November equatorial Pacific, and 1.5°C for the December–February equatorial Pacific). Similarly, the anomaly fields used in the cold episode reconstructions are the regression coefficients multiplied by the average SST anomaly index for the 5 coldest years on record (−1.6°C for Pt. Chicama and −0.8°C for the equatorial Pacific). The positive skewness of the SST indices is evident in Fig. 1; however, it is not large enough to invalidate the linear regression analysis approach adopted here (see Deser 1989). Sadler et al.'s (1987) long-term monthly mean SST, pres-

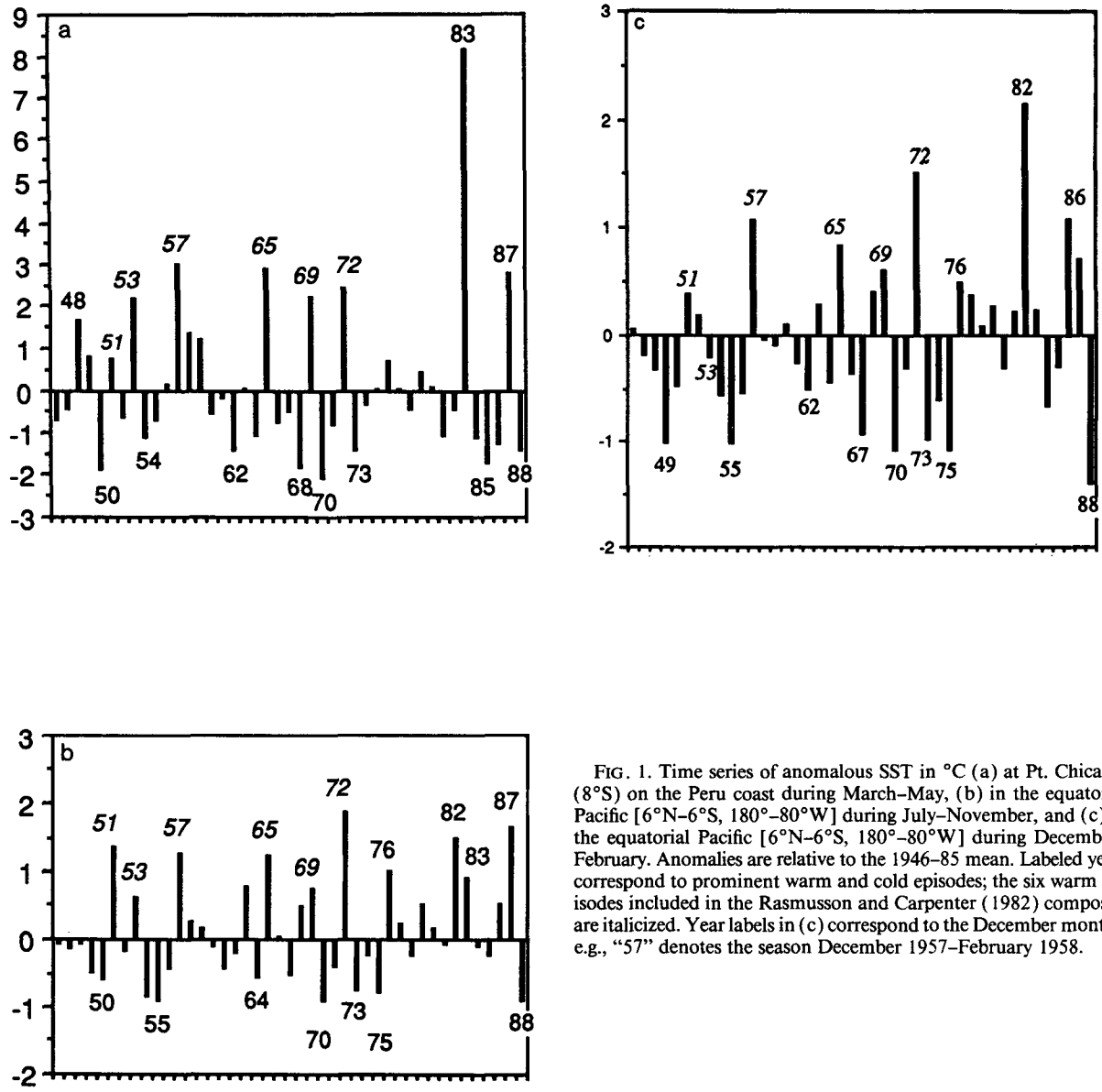

FIG. 1. Time series of anomalous SST in °C (a) at Pt. Chicama (8°S) on the Peru coast during March–May, (b) in the equatorial Pacific [6°N–6°S, 180°–80°W] during July–November, and (c) in the equatorial Pacific [6°N–6°S, 180°–80°W] during December–February. Anomalies are relative to the 1946–85 mean. Labeled years correspond to prominent warm and cold episodes; the six warm episodes included in the Rasmusson and Carpenter (1982) composite are italicized. Year labels in (c) correspond to the December months: e.g., "57" denotes the season December 1957–February 1958.

sure, and surface wind fields were used as climatology. The OLR climatology is based on the period 1974–89.

The frequency of marine surface observations over the tropical Pacific is documented by RC and Wright et al. (1987). In dealing with the data-sparse regions, one must either perform some kind of interpolation and smoothing (as in RC) or leave some regions blank (as in Wright et al. 1987). In the present study, we have interpolated and smoothed the fields in the data-sparse regions through the following procedures. First the seasonal mean anomaly fields for each year were smoothed in the east-west direction by averaging the data in each 2° square with the two grid boxes immediately to the east and west. The contribution of each individual 2° square to this 10° average was weighted by the number of observations. If the central grid box contained no data, averaging was not performed. Values for missing grid boxes were obtained by linear interpolation in the east-west direction after smoothing. If more than 10 adjacent 2° squares had missing values, interpolation was not performed. A regression coefficient was then calculated for each 2° square for which at least 15 years of data were available. In practice, all of the gridboxes except those over the southeastern Pacific contained at least 30 years of data after interpolation.

The regression coefficients were smoothed in the east-west direction with a 5-point (10° of longitude) moving average. The 2° north–south resolution of the original data was retained in all of the regression fields

except sea level pressure. An additional smoothing in the north–south direction with a 3-point moving average was applied to the pressure regression fields that were more noisy. In order to retain more of the small scale structure in the SST field near the South American coast, the March–May SST anomaly and regression fields were smoothed in the east–west direction with a 3- instead of a 5-point moving average.

Even after applying the procedures described above, the fields in regions of weak gradients contained spurious features such as cusps and "figure 8's" introduced by the contouring routine that would have been smoothed out by a skilled hand analyst. In order to eliminate these features we made a number of small adjustments to some of the gridpoint values. Fewer than 5% of the grid points over the tropical Pacific were manually altered, and these corrections amounted to less than 0.1°C for SST, 0.1 mb for sea level pressure, 0.1°C for sea–air temperature difference, 0.3% for relative humidity and 0.1 oktas for cloud amount, all of which are comparable to the uncertainties inherent in these fields. No smoothing was performed on the OLR data.

3. Coastal warm and cold episodes

a. March–May anomaly fields (Fig. 2)

Regressions of March–May SST, surface wind, and OLR upon the Pt. Chicama SST index are shown in Fig. 2. Multiplying these regressions by 2.6° (−1.6°) yields anomaly fields representative of the 5 strongest warm (cold) episodes along the Peru coast during the period 1946–85, as discussed in section 2. The most coherent features are observed east of 140°W.

The largest SST anomalies (upper panel) are observed along the Peru coast between 4° and 12°S. Weaker anomalies extend along the equator from the coast of South America to ~130°W. The equatorial and coastal SST anomalies are highly correlated ($r = 0.9$)[1] with Pt. Chicama SST. The distribution of SST anomalies closely resembles the RC composite for the 'Peak Phase' and the standard deviation associated with the interannual variability of March–May SST (not shown).

Northerly wind anomalies are observed between 2° and 8°N with weaker southerly anomalies between the equator and 4°S. These meridional wind anomalies converge over the equatorial SST anomalies in a simple thermally direct circulation. The anomalous northerly winds are located over and just to the south of the climatological mean position of the Inter Tropical Convergence Zone (ITCZ) during March–May. Correlations between the northerly and southerly wind anomalies and Pt. Chicama SST are ~0.7 and 0.5, respectively. The surface wind regressions are consistent with the RC composite, although the meridional wind anomalies between 110°W and the South American coast are more apparent in our analysis. In agreement with Wyrtki (1975), Ramage and Hori (1981) and RC, the wind anomalies off the Peru coast are weak and poorly correlated with Pt. Chicama SST. As in the RC composite, westerly wind anomalies are observed in the central equatorial Pacific, but the correlation coefficients associated with them are small ($r = 0.4$). In fact, two of the most prominent March–May warm episodes, 1957 and 1965, were accompanied by slight *easterly* anomalies in the central equatorial Pacific (not shown).

A narrow band of negative OLR regression coefficients (lower panel), indicative of enhanced convection during warm episodes, is centered along 2°–3°N. These anomalies extend westward to the dateline. Meridional wind anomalies converge into the region of enhanced convection. The negative OLR anomalies are highly correlated with Pt. Chicama SST ($r = -0.9$), but it should be remembered that this result is based on a limited sample of years (14). The OLR regressions are consistent with enhanced rainfall at the Galapagos Islands (0°, 90°W) during warm episodes. It is interesting to note that while torrential rains are often reported along the coasts of Peru and Ecuador during March–May warm episodes, the negative OLR regressions suggest that the anomalous precipitation is even greater over the ocean than over the South American littoral.

The March–May sea level pressure regression field (not shown) exhibits a nearly uniform distribution of negative pressure anomalies in the eastern Tropical Pacific, with values ~ −0.2 mb per °C of the SST index between 8°N and 20°S, east of 130°W. The correlation between pressure averaged over the area defined above and Pt. Chicama SST is ~ −0.6.

b. March–May cold episode total fields (Fig. 3)

The SST distribution (upper panel) is characterized by cold upwelling zones along the Peru coast and the equator and a fairly pronounced Equatorial Front along 3°N that separates the equatorial "cold tongue" from the warmer waters of the North Equatorial Counter Current. The confluence of the southeast and northeast trades is observed ~5°–7°N, over the narrow band of high SST west of 110°W and along the southern edge of the warm pool off Central America, with maximum convergence ~ -7×10^{-6} s^{-1}. The OLR field (lower panel) exhibits a minimum, which corresponds to a maximum in deep convective clouds, along this band of convergence. The OLR minimum is separated into two centers: one along 7°N that extends across the basin westward of 110°W, and another just to the west of Colombia, south of the warm pool. A secondary convergence zone occurs within the southeast trades, as evidenced by the marked deceleration of the winds

[1] The notation "$r = 0.9$" is used throughout the text to indicate the value of the correlation coefficient, r, between two time series.

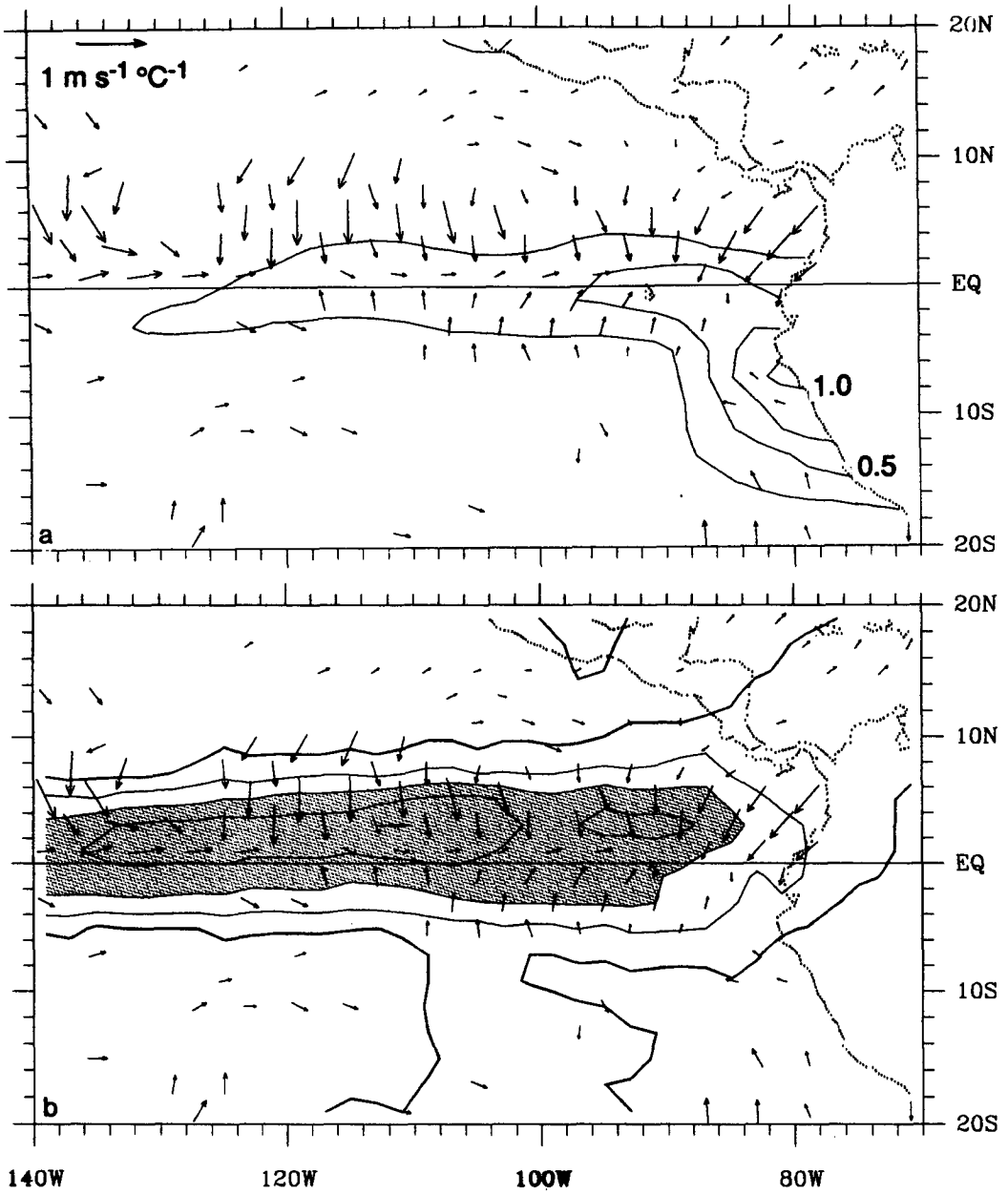

FIG. 2. (a) Regressions of March–May SST and surface wind upon the Pt. Chicama SST index, based on the period 1946–85 (1983 excluded). SST regression coefficients are contoured every 0.25°C per °C of the SST index. Wind vectors are shown only for those grid points whose u or v correlations with the SST index exceed 0.3 in absolute value. (b) As in (a) but for outgoing longwave radiation (OLR) and surface wind. OLR regressions are based on the period 1974–89 (1978 missing and 1983 excluded). OLR regression coefficients are contoured every 2.5 W m^{-2} per °C of the SST index; the zero contour is darkened and regression coefficients less than -5 W m^{-2} $°C^{-1}$ are shaded.

across 5°S between 110° and 90°W, along the band of warm water immediately to the south of the equatorial cold tongue. Maximum convergences within this zone are $\sim -3 \times 10^{-6}$ s^{-1}. This feature is consistent with local maxima in cloudiness and precipitation frequency (Hastenrath and Lamb 1977) and cloud brightness measurements from satellites (Gruber 1972). It is also reflected as a relative minimum in OLR, but values along 5°S are above our contouring threshold. The two convergence zones are separated by a band of divergence ~1°N along the northern edge of the cold tongue where the wind speed increases in the downstream direction. This equatorial divergence, with maximum values $\sim 3 \times 10^{-6}$ s^{-1}, is consistent

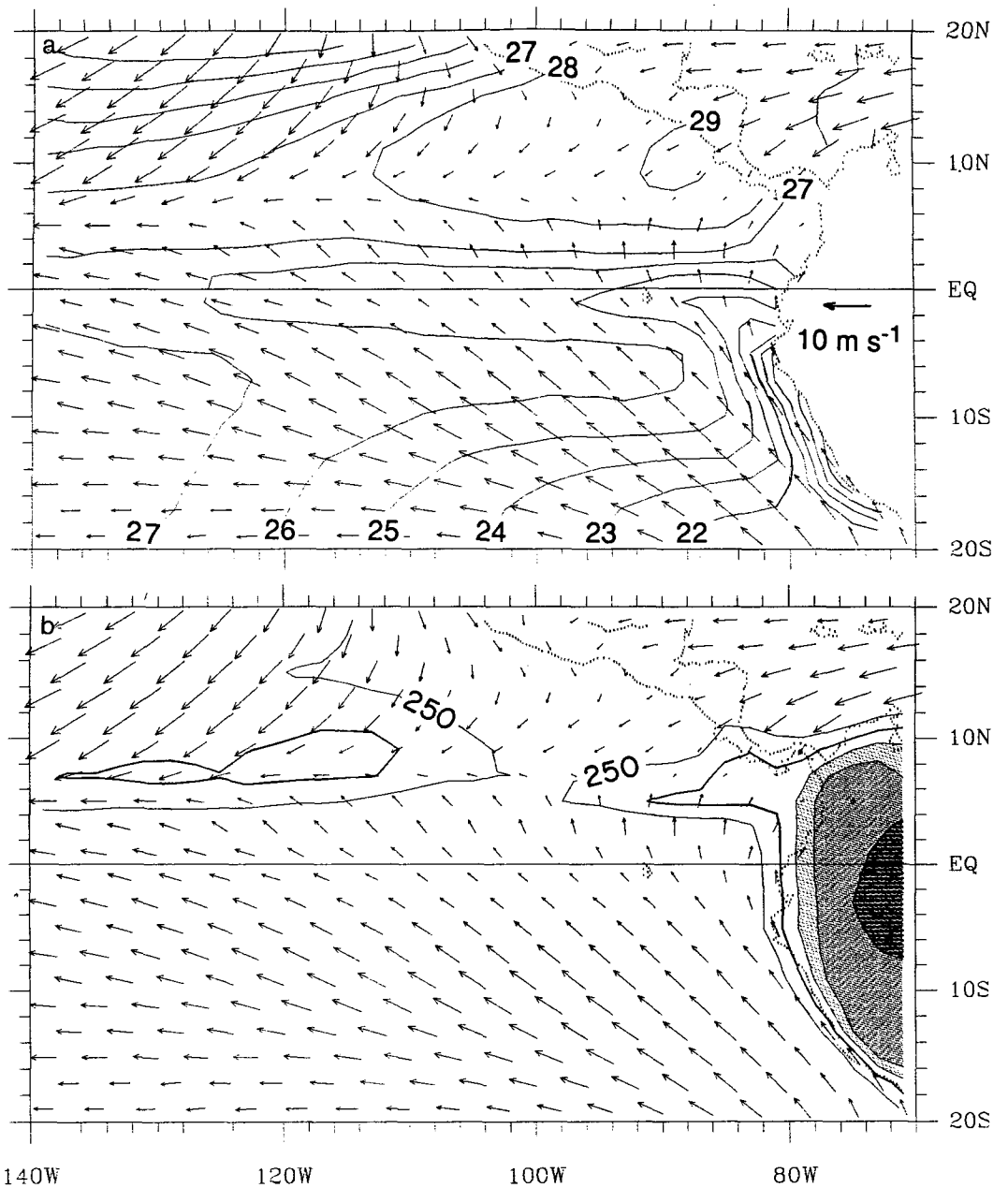

FIG. 3. (a) March–May total SST (°C) and surface wind composites for a typical cold episode along the Peru coast. Composites are based upon regressions as described in section 2. (b) As in (a) but for OLR (W m^{-2}) and surface wind. OLR values are contoured every 10 W m^{-2}; the 240 W m^{-2} contour is darkened and values < 230 W m^{-2} are shaded. OLR values < 260 W m^{-2} not contoured.

with the light rainfall amounts (<5 cm total) at the Galapagos Islands during cold March–May seasons (Taylor 1973).

c. *March–May warm episode total fields (Fig. 4)*

In the warm March–May composite, a vestige of the equatorial cold tongue is observed ~1°S, but SSTs are only a few tenths of a degree cooler than over the surrounding waters. The Equatorial Front is barely discernable. Upwelling of cold water is still evident along the coasts of Ecuador and Peru, but the temperature contrast between the coastal and offshore waters is weaker than in the cold composite. A tongue of warm water about 500 km off the coast of Peru protrudes farther southward than during the cold years. The southerly winds to the north of the equator in the east-

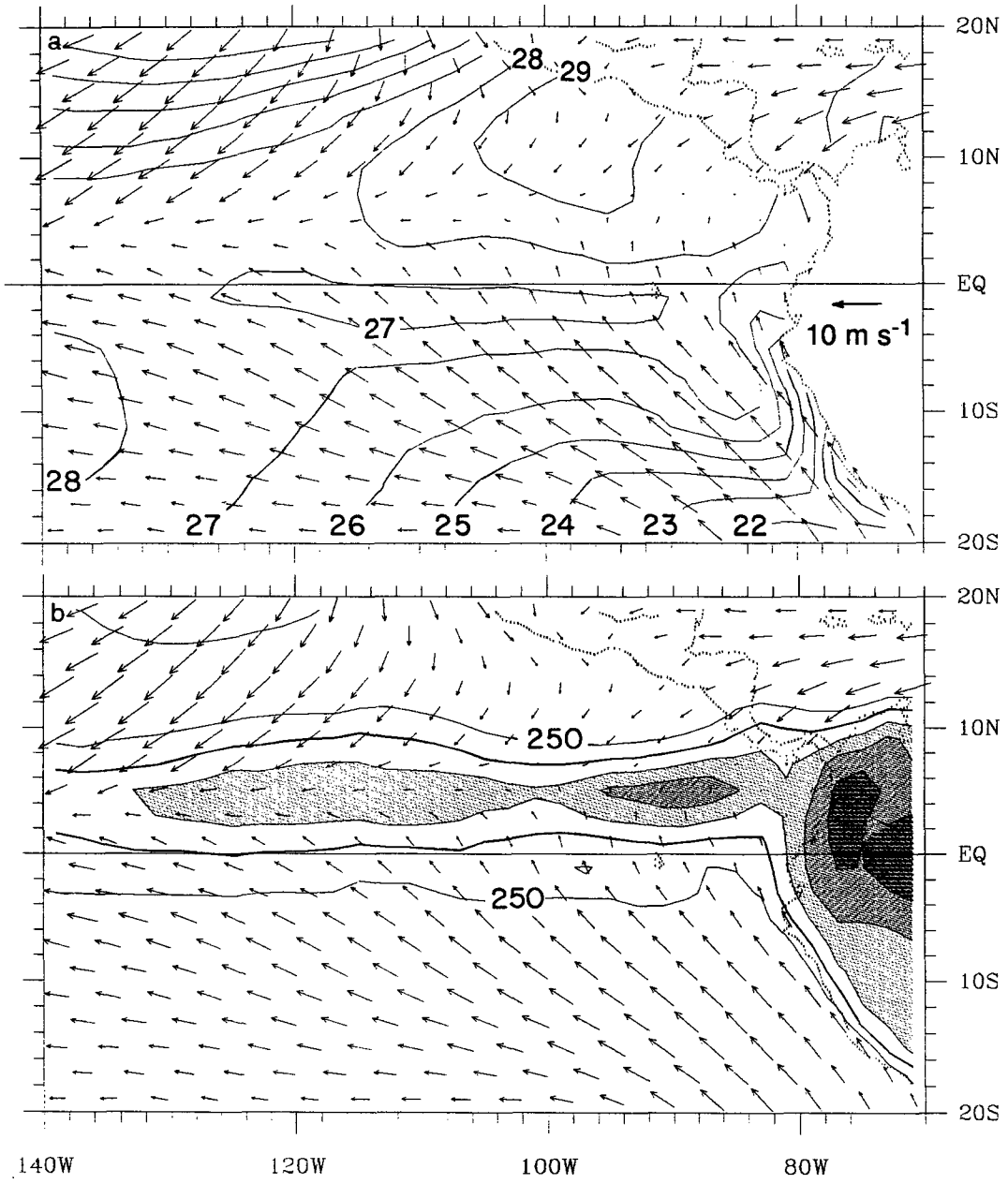

FIG. 4. As in Fig. 3 but for a typical warm episode along the Peru coast.

ern Pacific and the equatorial easterlies westward of 130°W are weaker than in the cold composite. The southeast trades decelerate uniformly as they pass from the southern subtropics to ~4°N; maximum convergence is found between 2°N and 6°N.

The OLR field (lower panel) exhibits a well defined ITCZ along 5°N, coincident with the region of strongest surface wind convergence. The lowest OLR values within the ITCZ are ~225 W m^{-2}, as opposed to ~235 W m^{-2} in the cold composite.

It is interesting to compare the warm episode of March–May 1983 (not shown), during which Pt. Chicama SST was 8°C above normal (Fig. 1), with the composite warm episode. Like the composite, the 1983 warm episode features a narrow tongue of warm water ~500 km off the Peru coast. However, there is no trace of the equatorial cold tongue during March–May 1983: SSTs are uniformly high (28°C–29°C) within ~10° of the equator. Consistent with the SST distribution, the ITCZ in March–May 1983 is centered along the equator and is more intense (minimum OLR values ~205 W m^{-2}) than in the composite (see Deser 1989).

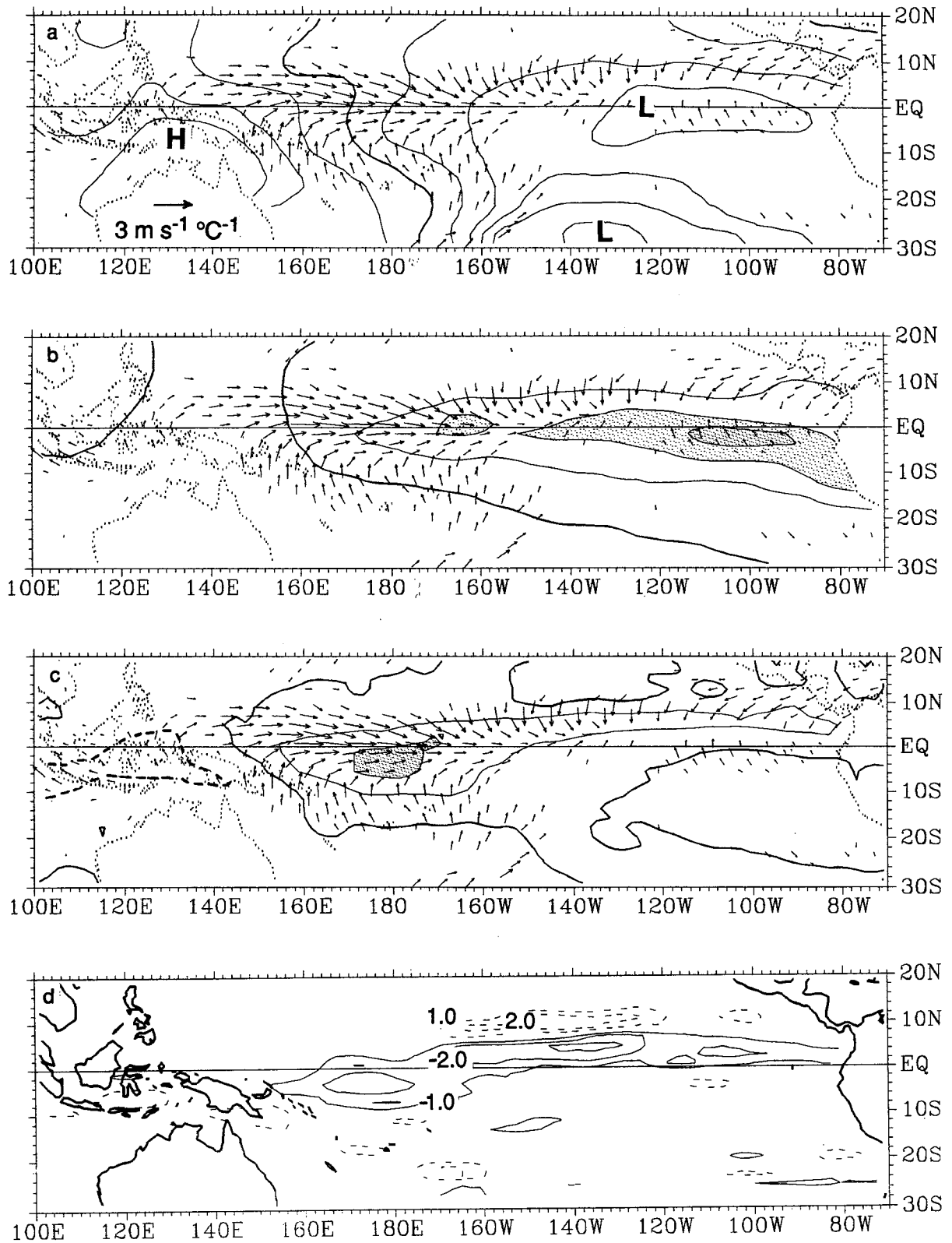

FIG. 5. (a) Regressions of July–November sea level pressure and surface wind upon the equatorial SST index (defined as July–November SST averaged over 6°N–6°S, 180°–80°W), based on the period 1946–85. Contour interval = 0.25 mb per °C of the SST index; the zero contour is darkened. Wind vectors are shown only for those grid points whose u or v correlations with the SST index

4. Basin-wide warm and cold episodes

a. *Anomaly fields*

1) JULY–NOVEMBER (FIG. 5)

Regressions of July–November sea level pressure, SST, surface wind and OLR on the equatorial Pacific SST index are shown in Fig. 5. Multiplying these regressions by 1.4° (−0.8°) yields anomaly fields representative of the 5 strongest warm (cold) episodes during the period 1946–85, as discussed in section 2.

The Southern Oscillation, a basin-wide pattern consisting of below normal pressure over the Southeast Pacific Ocean and above normal pressure over northern Australia and Indonesia, shows up clearly in Fig. 5a. Both centers of action are well correlated with our equatorial Pacific SST index ($|r| = 0.8$). There is a distinct secondary maximum of below normal pressure in a narrow band along the equator in the eastern Pacific; these pressure anomalies are highly correlated ($r = -0.9$) with the SST index. The anomalous zonal pressure gradient along the equator is centered over the western Pacific. The large-scale features of the pressure regression field are in good agreement with previous studies of the Southern Oscillation by Troup (1965), Trenberth (1976), Wright (1977) and others based on station pressure records and by Barnett (1985) and Wright et al. (1988) from ship observations. The distinct secondary maximum of anomalous pressure in the equatorial eastern Pacific appears to be a new finding.

Westerly wind anomalies are observed over the western equatorial Pacific, directed down the anomalous zonal pressure gradient. These anomalies are in agreement with Harrison's (1987) results based on island winds. The orientation of the surface meridional winds relative to the isobars is generally consistent with a transition from Ekman balance in the subtropics to down-gradient flow along the equator. Southerly wind anomalies are observed to the south of the equator in the western Pacific and a narrow band of northerly wind anomalies between 6° and 10°N is found over the eastern Pacific. These regions of anomalous northerly and southerly winds coincide with the mean positions of the ITCZ and South Pacific Convergence Zone (SPCZ), respectively. Northeasterly anomalies are observed off Central America. A coherent region of southerly wind anomalies is found in the eastern equatorial Pacific, centered ~1°S where no anomalous pressure gradient is observed; this feature is discussed in detail by Wallace et al. (1989). The features in the surface wind regression field discussed above are all well correlated with the SST index ($|r| > 0.7$) and are consistent with the RC composite.

TABLE 1. Simultaneous correlation coefficients between regional indices of surface wind (u, v) and sea level pressure (P) and the July–November equatorial Pacific SST index during 1946–85. Also shown are the correlation coefficients between the wind indices and pressure *difference* indices, denoted by $r(u, Pw - Pe)$.

u	Pw	Pe	
4°N–6°S	6°N–6°S	6°N–6°S	
150°E–150°W	100°–150°E	150°–84°W	$r(u, Pw - Pe) = 0.9$
0.8	0.8	−0.9	
v	Pn	Ps	
12°–4°N	20°–12°N	6°N–6°S	
160°–80°W	150°–84°W	150°–84°W	$r(v, Pn - Ps) = -0.9$
−0.8	−0.5	−0.9	
v	Pw	Pe	
6°–20°S	6°–20°S	6°–20°S	
150°E–160°W	100°–150°E	160°–84°W	$r(v, Pw - Pe) = 0.9$
0.7	0.8	−0.8	

Table 1 provides more quantitative information on the strengths of the simultaneous correlation coefficients between the July–November SST index and surface wind and sea level pressure anomalies in selected regions. The regional indices were formed by averaging the data from each 2° square, weighted by the number of observations, within the selected areas. The correlation coefficients between the surface winds and pressure gradients reach 0.9 in absolute value for all three indices; this high degree of correlation lends further credence to the regression fields displayed in Fig. 5.

Positive SST regression coefficients (Fig. 5b) extend from the dateline to the South American coast, as in the RC composite. The largest anomalies occur ~2°S between 90°W and 110°W. Anomalous southerly winds are observed over the largest SST anomalies. Westerly wind anomalies are confined to the western edge of the region of positive SST anomalies. The largest SST anomalies roughly coincide with the secondary maximum of below normal pressure along the equator in the eastern Pacific.

The OLR regression field (Fig. 5c) exhibits a narrow band of negative values, indicative of increased atmospheric convection during warm episodes, across the central and eastern Pacific, centered ~5°N. This feature is associated with a southward expansion and intensification of the ITCZ during warm episodes. A

exceed 0.4 in absolute value. (b) As in (a) but for SST and surface wind. Contour interval = 0.5°C per °C of the SST index; the zero contour is darkened and regression coefficients > 1°C per °C are shaded. (c) As in (a) but for OLR and surface wind. OLR regressions are based on the period 1974–89 (1978 missing). Contour interval = 10 W m^{-2} per °C of the SST index; the zero contour is darkened and the positive contour is dashed. Values < −20 W m^{-2} per °C are shaded. (d) Divergence of surface wind regressions shown in (a) in units of 10^{-6} s^{-1} °C^{-1}. Solid (dashed) contours indicate anomalous wind convergence (divergence) during warm episodes.

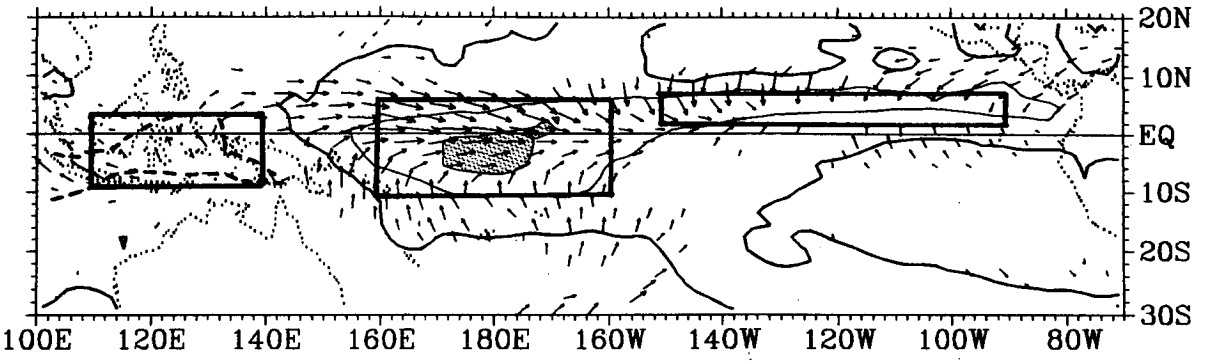

FIG. 6. As in Fig. 5c. Boxes outline regional indices of OLR and surface wind divergence referred to in Table 2.

couplet consisting of negative OLR regression coefficients in the equatorial western Pacific and weaker positive regression coefficients over Indonesia, is also apparent in Fig. 5c. This pattern is associated with an eastward shift and intensification of the equatorial convection during warm episodes. It may be noted that there is a net decrease in OLR (or a net increase in deep convective cloudiness) over the tropical Pacific during warm episodes. The OLR patterns are highly correlated with the SST index ($|r| \sim 0.9$). The OLR regression coefficients in the western equatorial Pacific and over Indonesia are corroborated by cloudiness observations from the COADS (not shown) and by rainfall records at island stations [Doberitz (1968), Wright et al. (1988), and Kiladis and van Loon (1988)].

The distribution of anomalous surface wind divergence during July–November warm episodes is shown in Fig. 5d. A narrow band of convergence extends across the central and eastern Pacific, centered ~5°N, with maximum values of -0.7×10^{-6} s^{-1} per °C of the SST index (hereafter, 'units' will be used in place of '$\times 10^{-6}$ s^{-1} per °C of the SST index'). Weaker convergence (maximum values ~ −0.3 units) is observed in the western Pacific from 2°N to 8°S between 160°E and 160°W. A narrow band of divergence is observed along 10°N in the central Pacific. It should be emphasized that meridional wind anomalies dominate the anomalous surface wind convergence field, even over the western equatorial Pacific, because the meridional scale of the major features in the wind pattern are so much smaller than the zonal scale.

There is remarkable correspondence between the regions of negative OLR regressions and the areas of convergence in the surface wind regression field (compare Figs. 5c and d) but the band of divergence along 10°N from 170° to 120°W is not accompanied by large positive OLR regression coefficients. As a quantitative comparison of the surface wind convergence and OLR anomalies during warm episodes, we computed regression coefficients for OLR and surface wind convergence for three regions outlined in Fig. 6. The results, summarized in Table 2, show that the ratio of OLR to surface wind convergence regression coefficients is a factor of two to three larger over Indonesia and the western equatorial Pacific than over the eastern Pacific. Since specific humidity varies by only 10%–15% across the equatorial Pacific, this difference is indicative of a deeper layer of convergence in the west than in the east.

2) DECEMBER–FEBRUARY (FIG. 7)

Regressions of December–February sea level pressure, SST, surface wind and OLR on the equatorial Pacific SST index are shown in Fig. 7. Multiplying these regressions by 1.5° (−0.8°) yields anomaly fields representative of the 5 strongest warm (cold) episodes during the period 1946–85, as discussed in chapter 2.

The Southern Oscillation continues to be prominent in the pressure regression field (Fig. 7a). However, several changes from the July–November pattern are evident:

1) the development of positive pressure anomalies in the subtropical western Pacific of both hemispheres

TABLE 2. Simultaneous regression coefficients for July–November regional averages of OLR and surface wind divergence ($\nabla \cdot V$) upon the equatorial Pacific SST index. See Fig. 6 for region locations.

	Eastern Pacific 8°–2°N 150°–90°W	Western Pacific 6°N–10°S 160°E–160°W	Indonesia 4°N–8°S 110°–140°E	
OLR	−11.3	−15.0	10.1	W m^{-2} °C^{-1}
$\nabla \cdot V$	−1.4	−0.8	0.3	10^{-6} s^{-1} °C^{-1}
OLR/$\nabla \cdot V$	8.0	18.0	29.0	10^{6} W m^{-2} s^{-1} °C^{-1}

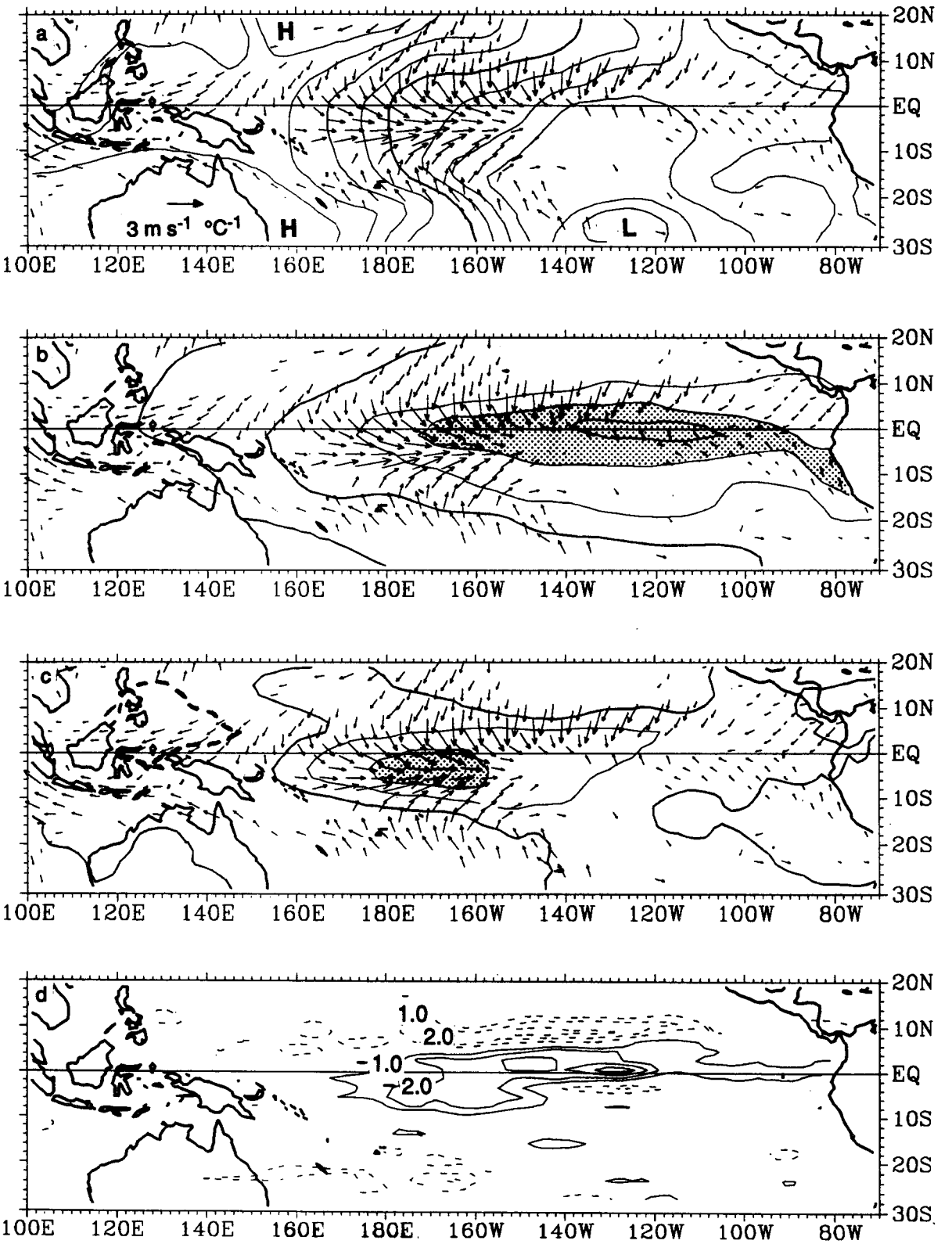

FIG. 7. Regressions of December–February (a) sea level pressure and surface wind, (b) SST and surface wind, (c) OLR and surface wind, and (d) surface wind divergence upon the equatorial SST index (defined as December–February SST averaged over 6°N–6°S, 180°–80°W). Plotting convention as in Fig. 5.

and an increase in the amplitude of the positive pressure anomalies over the equatorial western Pacific and northern Australia,

2) the strengthening of the zonal pressure gradient along the equator near the dateline. These differences have been noted by Wright et al. (1988) and others.

The development of anomalous subtropical anticyclones over the western Pacific is accompanied by anomalous equatorward flow between 10° and 20° in both hemispheres over the central Pacific. The tightening of the anomalous zonal pressure gradient over the equatorial western Pacific is accompanied by stronger westerly wind anomalies. These zonal wind anomalies are centered ~6°S rather than at the equator as in the July–November pattern. The southward shift of the surface westerly wind anomalies in the central Pacific is consistent with Harrison's (1987) results based on island wind data. A narrow band of northerly wind anomalies associated with the ITCZ continues to be observed over the central Pacific near 5°N. The wind anomalies over the far eastern tropical Pacific have weakened relative to the July–November season. Over the far western equatorial Pacific, the wind anomalies are northeasterly rather than westerly as in July–November. The December–February wind regression field is in close agreement with the RC composite. With the exception of the meridional wind anomalies between 10°N and 20°N in the central Pacific, all of the features of the wind regression field mentioned above exhibit correlations with the SST index stronger than 0.7 in absolute value.

Table 3 lists simultaneous correlation coefficients between the December–February equatorial SST index and surface wind and pressure in selected regions and between the surface winds and pressure gradients themselves. The surface winds are strongly correlated with the pressure gradients and with the SST index in all three regions. Note that the meridional winds near 5°N are well correlated with the north–south pressure gradient even though pressure in each individual region is only weakly correlated with the SST index. Pressures over the eastern Pacific (equatorial and southern subtropics) are only weakly correlated with the SST index in December–February.

TABLE 3. Simultaneous correlation coefficients between regional indices of surface wind (u, v) and sea level pressure (P) and the December–February equatorial Pacific SST index during 1946–85. Also shown are the correlation coefficients between the wind indices and pressure *difference* indices, denoted by $r(u, Pw - Pe)$.

u	Pw	Pe	
2°N–10°S	2°N–10°S	2°N–10°S	$r(u, Pw - Pe) = 0.9$
164°E–152°W	100°–164°E	152°–80°W	
0.8	0.8	−0.7	
v	Pn	Ps	
10°– 2°N	20°–10°N	2°N–10°S	$r(v, Pn - Ps) = -0.8$
180°–118°W	180°–118°W	180°–118°W	
−0.9	0.2	−0.5	
v	Pw	Pe	
10°– 22°S	10°–22°S	10°–22°S	$r(v, Pw - Pe) = 0.8$
170°E–150°W	100°–170°E	150°–80°W	
0.8	0.8	−0.6	

Positive SST regression coefficients (Fig. 7b) extend along the equatorial upwelling zone from the dateline to 100°W, as in the RC composite. The largest positive SST anomalies are observed between 140° and 110°W, centered at the equator. The SST anomalies have strengthened in the central Pacific and weakened east of 110°W relative to July–November. Westerly wind anomalies continue to be confined to the western edge of the region of positive SST anomalies.

The OLR regression field (Fig. 7c) features a broad region of negative values over the central equatorial Pacific and an area of weaker positive values over Indonesia, centered to the north of the equator. The negative OLR anomalies, indicative of increased convective activity during warm events, extend farther to the east along the equator than in July–November. The latitudinal position of the strongest negative OLR anomalies is almost the same in the two seasons; however, in July–November the strongest westerly wind anomalies are along the northern fringe of the negative OLR anomalies, whereas in December–February they run along the southern fringe. The OLR anomalies over the far eastern Pacific have weakened relative to those in July–November.

There is good correspondence between the regions of anomalous surface wind convergence and negative OLR anomalies (Fig. 7d); As in July–November, the anomalous surface wind convergence field is dominated by the meridional wind component. The narrow band of anomalous divergence near 10°N is not associated with positive OLR anomalies and the region of positive OLR anomalies over Indonesia is not associated with strong anomalous surface wind divergence.

b. *Cold episode total fields*

1) JULY–NOVEMBER (FIG. 8)

We have chosen to describe the composite charts for the total July–November fields in terms of eastern, central, and western Pacific climatic regimes, which vary in strength and longitudinal extent from year to year.

Eastern Pacific regime (~120° W to the coast of South America)

The eastern equatorial Pacific is characterized by large meridional gradients of sea level pressure and SST

and by southerly surface winds. The sea level pressure field (top panel) is dominated by the strong Subtropical High that extends northward across the equator and westward into the central South Pacific. The Southeasterly Trades diverge out of the Subtropical High and become predominantly southerly as they cross into the Northern Hemisphere. Air parcels decelerate as they approach the equator from the south, reaching minimum speeds at 1°S, and then rapidly accelerate north of the equator, reaching maximum speeds near 4°N. The strengthening of the southerly winds north of the equator may be a response to the increased northward pressure gradient force (the meridional Coriolis force is negligible in this region) and the changing stability characteristics of the planetary boundary layer (Wallace et al. 1989). The SST distribution (middle panel) is characterized by a prominent cold tongue centered at 1°S and a sharp meridional temperature gradient between the equator and 5°N. The ocean general circulation modeling experiments of Philander and Pacanowski (1981) indicate that southerly wind stress may be responsible for the oceanic frontal zone centered just to the north of the equator in the eastern Pacific. The meridional sea level pressure gradient is enhanced over the oceanic frontal zone, although it is somewhat broader in meridional scale than the SST gradient. Minimum surface wind speeds coincide with the coldest waters at 1°S, while maximum speeds are observed ~2° north of the strongest meridional SST gradient. As a consequence, strong surface wind divergence (maximum values of 7×10^{-6} s^{-1}) is centered directly over the oceanic frontal zone, several degrees to the

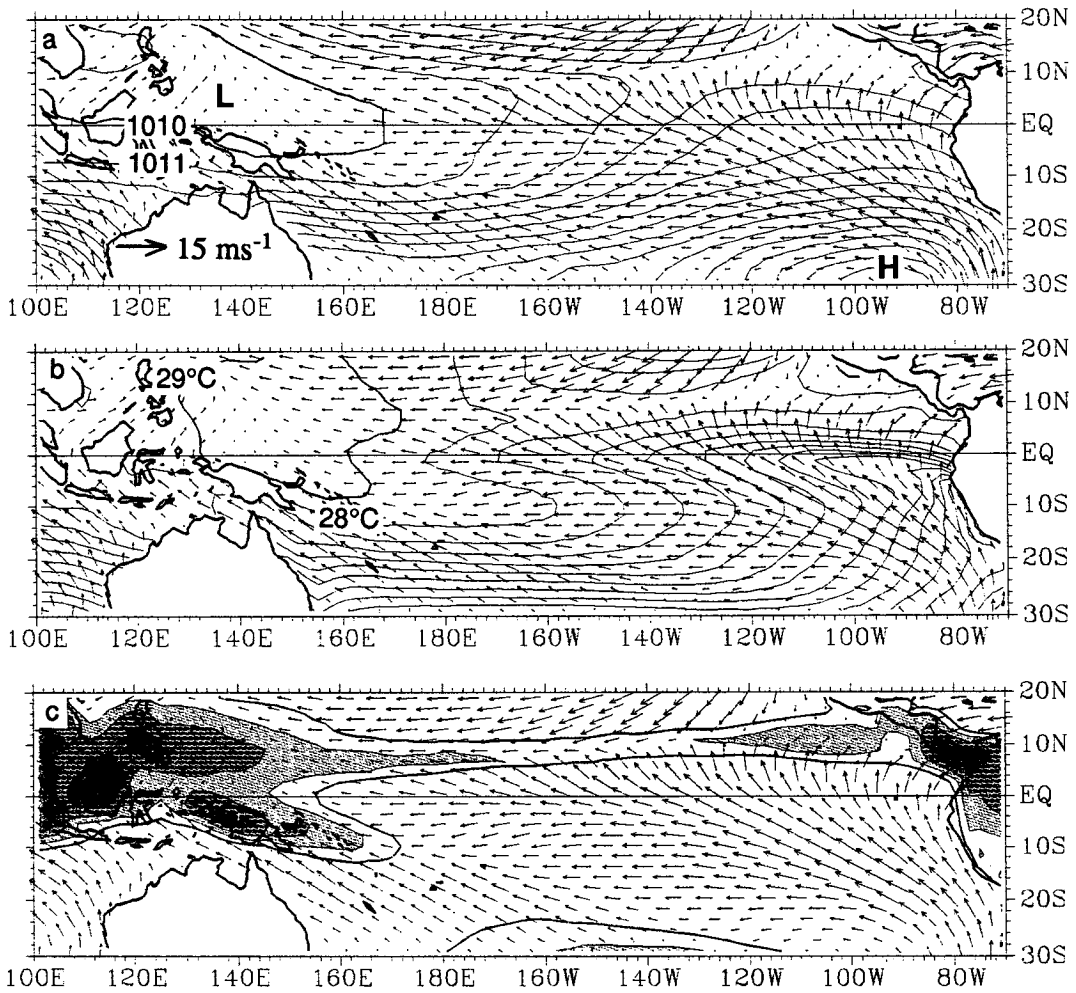

FIG. 8. (a) July–November total sea level pressure and surface wind composites for a typical cold episode in the eastern equatorial Pacific. Composites are based upon regressions as described in Section 2. Contour interval = 1 mb. (b) As in (a) but for SST and surface wind. Contour interval = 1°C. (c) As in (a) but for OLR and surface wind. Contour interval = 10 W m^{-2}. The 240 W m^{-2} contour is darkened; values < 230 W m^{-2} are shaded, and values > 240 W m^{-2} are not contoured.

north of the coldest water. The ITCZ is marked by a narrow band of strong surface wind convergence (maximum values $\sim 8 \times 10^{-6}$ s^{-1}) and deep convection centered along ~11°N. East of 110°W, the maximum surface convergence is observed within the southerly flow and lies ~2° south of the OLR minimum. The strongest convection is located over Panama and northwestern Colombia.

Central Pacific regime (180° to ~140°W)

In the central Pacific, the SST distribution is nearly symmetric about the equator with minimum temperatures centered on the equator itself rather than distinctly to the south of the equator as in the eastern Pacific regime. Zonal gradients of SST and surface pressure are strong along the equator driving easterly surface winds that cause equatorial upwelling across the central Pacific to beyond 160°E.[2] This easterly flow over the cold tongue is noticeably diffluent in response to the variation of the Coriolis parameter with latitude. The northward component of the pressure gradient force induces a bias toward northward flow, but unlike the eastern Pacific, the strength of the northward pressure gradient force is constant across the equator. Surface wind divergence is directly observed over the equatorial cold tongue, with maximum values $\sim 3 \times 10^{-6}$ s^{-1}. The strongest convergence (maximum values $\sim 9 \times 10^{-6}$ s^{-1}) is observed ~9°N, at the confluence of the northeast trades and the diffluent equatorial easterly flow. A secondary region of weaker surface convergence, with values on the order of 2×10^{-6} s^{-1}, is observed ~10°S, at the confluence of the southeast trades and the equatorial easterlies. The convergence associated with the ITCZ is located over the warmest waters while the convergence at 10°S lies near or slightly poleward of the axis of warmest water. The OLR distribution exhibits a narrow band of pronounced convection centered ~9°N, coincident with the region of surface wind convergence and warmest water. Deep convection does not appear to be associated with the region of weak convergence near 10°S.

Western Pacific regime (100°E to ~160°E)

The western Pacific is characterized by weak SST and surface pressure gradients, light mean surface winds, and strong convection. Lowest pressures and highest SSTs are observed to the north of New Guinea. Weak surface convergence ($<2 \times 10^{-6}$ s^{-1}) is observed throughout the region, while the strongest convection is found over Indonesia, centered north of the equator. Within this region, OLR values appear to be lower over the islands (Borneo, the Philippines, and New Guinea) than over the surrounding seas, even in these low-resolution data. The SPCZ extends southeastward from New Guinea. OLR exhibits a prominent maximum (indicative of reduced convective activity) in the equatorial dry zone between the ITCZ and SPCZ in the western Pacific. This feature is reflected in the surface wind divergence field (not shown) and agrees with the precipitation distribution from island stations during cold episodes (Kiladis and van Loon 1988).

Viewing the distributions of surface wind and OLR for the tropical Pacific as a whole, one notes that although the regions of surface wind convergence and low OLR generally coincide, the strongest surface convergence is associated with the ITCZ east of 170°W, while the lowest OLR values are observed over Indonesia where the surface wind convergence is much weaker. Differences in the vertical profiles of convergence between the two regions may account for this discrepancy, as discussed in section 6.

2) DECEMBER–FEBRUARY (FIG. 9)

The December–February cold composites exhibit many of the features observed during the previous season (July–November). Some of the major differences between the two seasons are highlighted below.

1) Both the lowest pressure and warmest SST in the western Pacific shift into the Southern Hemisphere in December–February. The lowest pressures are observed over northern Australia and a belt of low pressure extends eastward over the Coral Sea to Samoa. The highest SSTs are located to the east of New Guinea with warmer water than 29°C extending as far as the dateline at 10°S; farther east than in July–November.

2) The Indonesian monsoon convection has also shifted into the Southern Hemisphere and intensified. The distribution of convection in the western Pacific follows the highest SSTs, with the western edge of the equatorial dry zone located ~15° of longitude farther east than in July–November (as indicated by the 250 W m^{-2} contour). The SPCZ is more prominent than in July–November, as reflected not only in OLR but also in the surface wind field as the southeast Trades recurve toward the southwest in the central Pacific.

3) The convection associated with the ITCZ is not as strong in December–February as in July–November. However, strong convergence of the surface winds is still evident along 7°N in December–February.

c. Warm episode total fields

1) JULY–NOVEMBER (FIG. 10)

The three climatic regimes observed in the cold episode composites are still present during the warm ep-

[2] During July–November 1988, one of the strongest cold episodes on record (Fig. 1) and not included in this analysis, the equatorial cold tongue and surface easterlies extended to 150°E (Climate Diagnostics Bulletin 1988).

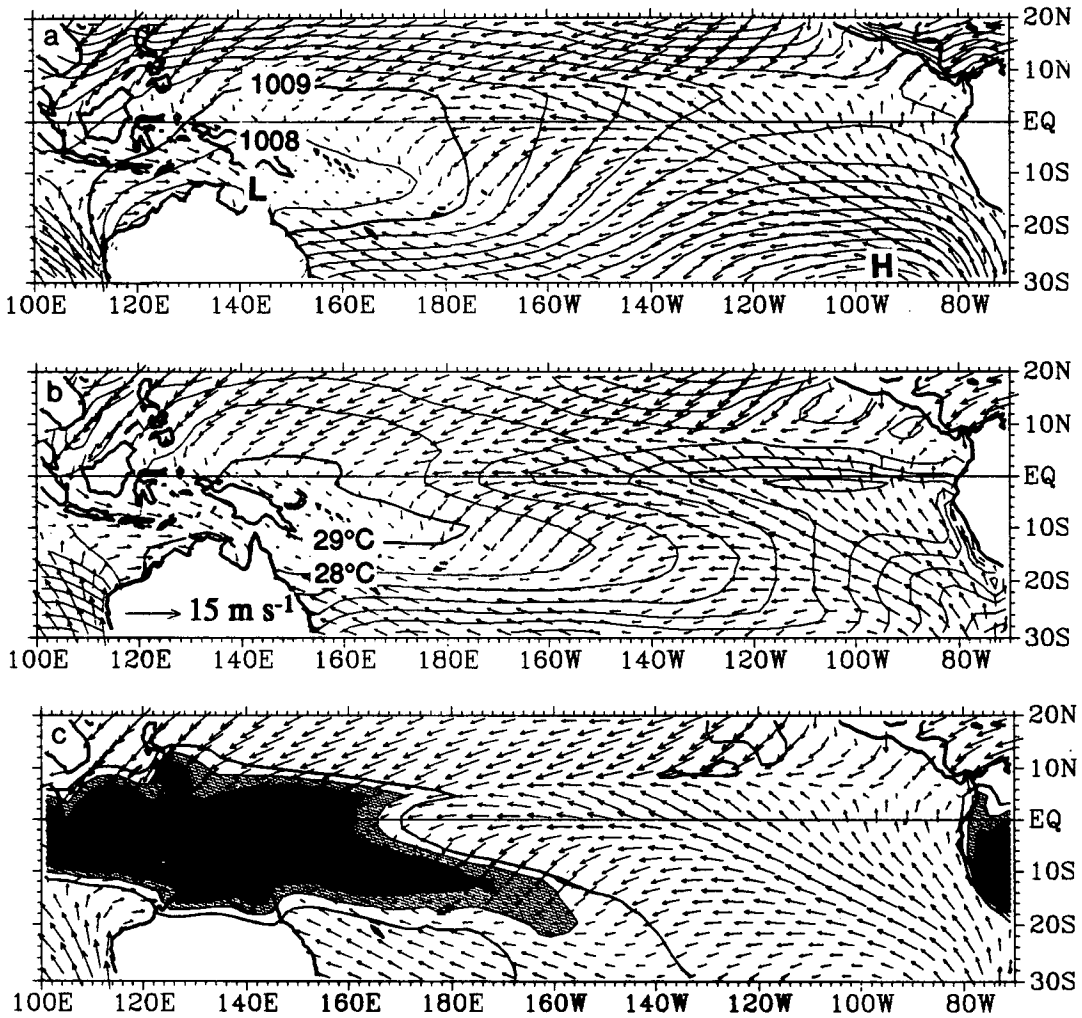

FIG. 9. December–February total (a) sea level pressure (mb) and surface wind, (b) SST (°C) and surface wind, and (c) OLR (W m^{-2}) and surface wind for a typical cold episode in the eastern equatorial Pacific. Plotting convention as in Fig. 8.

isodes, but the western Pacific regime has shifted eastward, consequently narrowing the zone occupied by the central Pacific regime.

Eastern Pacific regime

The sea level pressure distribution (top panel) is not dramatically different from its cold episode counterpart: However, the Subtropical High is weaker and its western and northern margins have receded. The SST gradient (middle panel) between the equator and 5°N is nearly a factor of two smaller than in the cold composite, as is the overlying meridional pressure gradient. Wind speeds are weaker at the northern edge of the southerly flow but stronger over the equator. The wind speed minimum over the cold tongue is barely discernible. As a result, surface wind divergence is less pronounced over the oceanic baroclinic zone (not shown). The area of convergence associated with the ITCZ extends ~2° of latitude farther southward, but the maximum convergence is weaker, so the total amount of convergence is comparable to that in the cold composite. Convection associated with the ITCZ (bottom panel) also extends farther southward, in agreement with the surface convergence field, and is more intense (minimum OLR values are ~10 W m^{-2} lower than in the cold composite). The strongest convection remains anchored over Panama and northwestern Colombia.

Central Pacific regime

The central Pacific regime now occupies only a narrow transition zone between ~160° and 140°W. It is

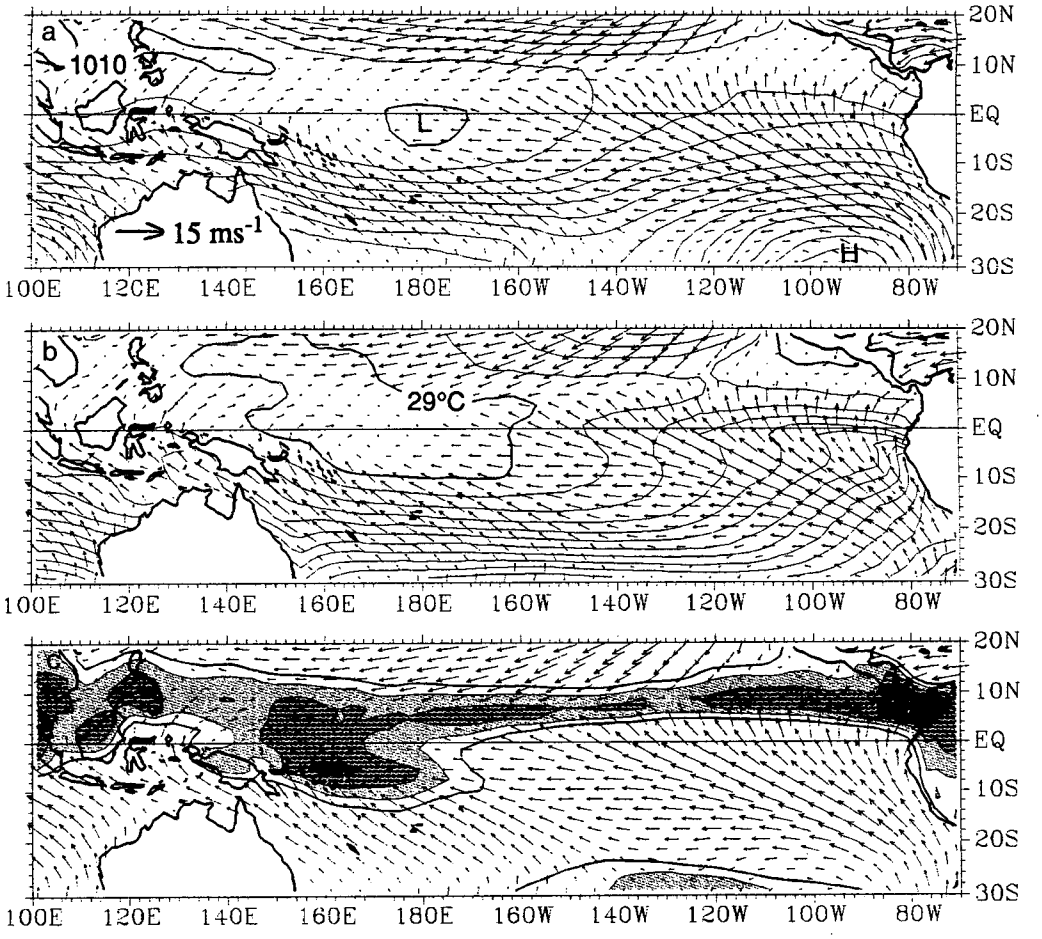

FIG. 10. July–November total (a) sea level pressure (mb) and surface wind, (b) SST (°C) and surface wind, and (c) OLR (W m^{-2}) and surface wind for a typical warm episode in the eastern equatorial Pacific. Plotting convention as in Fig. 8.

characterized by weaker zonal gradients of SST and pressure along the equator relative to the cold composite. Equatorial easterlies are weaker and extend only to the dateline, consistent with the pressure pattern. The SST minimum along the equator is less pronounced, in agreement with the smaller easterly wind stress. The northern branch of the equatorial diffluent flow extends to 6°N as compared to 8°N in the cold composite. Consequently, the area of surface wind convergence is broader; however, because the maximum convergence is weaker, the total convergence is comparable to that in the cold composite. The ITCZ, indicated by low OLR, extends several degrees of latitude farther southward in agreement with the surface convergence field. Within the ITCZ, OLR values are ~ 15 W m^{-2} less than in the cold composite, indicative of an intensification of the convection during warm episodes.

Western Pacific regime

The warmest water and lowest pressure are displaced eastward relative to the cold composite and are now centered near the dateline. Weak equatorial westerlies are observed between New Guinea and the dateline, centered ~3°N, consistent with the zonal pressure gradient. Southerly flow is evident between New Guinea and Borneo, in agreement with the meridional pressure gradient. Winds to the east of New Guinea and northern Australia exhibit a stronger southerly component. SSTs to the southeast of New Guinea are ~0.5°C cooler than in the cold composite in the area of enhanced surface wind speeds. OLR over Indonesia is higher than in the cold composite, indicative of less convective activity during warm episodes. As in the cold composite, lower OLR values are observed over the islands of Borneo, Philippines, and New Guinea

than over the surrounding seas. The convection associated with the SPCZ is more intense and displaced northeastward, with the minimum OLR located just north of the Solomon Islands. The wedge-shaped equatorial dry zone in the western Pacific is observed farther to the east (~170°W) and is less prominent than in the cold composite. Intense convection is observed over the equatorial western Pacific, consistent with the change from surface wind divergence to convergence (not shown) and with enhanced precipitation at island stations (Kiladis and van Loon 1988; Wright et al. 1988) during warm episodes.

2) DECEMBER–FEBRUARY (FIG. 11)

Notable features of the December–February warm episode composite include:

1) An eastward shift of the lowest pressure and warmest water, relative to the cold composite for the same season. An area of low pressure distinct from the one located over the Australian mainland is centered over the dateline at 6°S. SSTs warmer than 29°C now cover a broad expanse from New Guinea to 140°W between the equator and ~10°S.

2) An eastward shift of the Indonesian monsoon convection following the warmest water. The SPCZ is no longer separated from the monsoon convection.

3) An intensification of the ITCZ convection west of 120°W.

4) The complete disappearance of the equatorial cold tongue.

5. Sea–air temperature difference, relative humidity, and cloud amount

In this section we investigate the distributions of sea–air temperature difference, relative humidity, and cloud

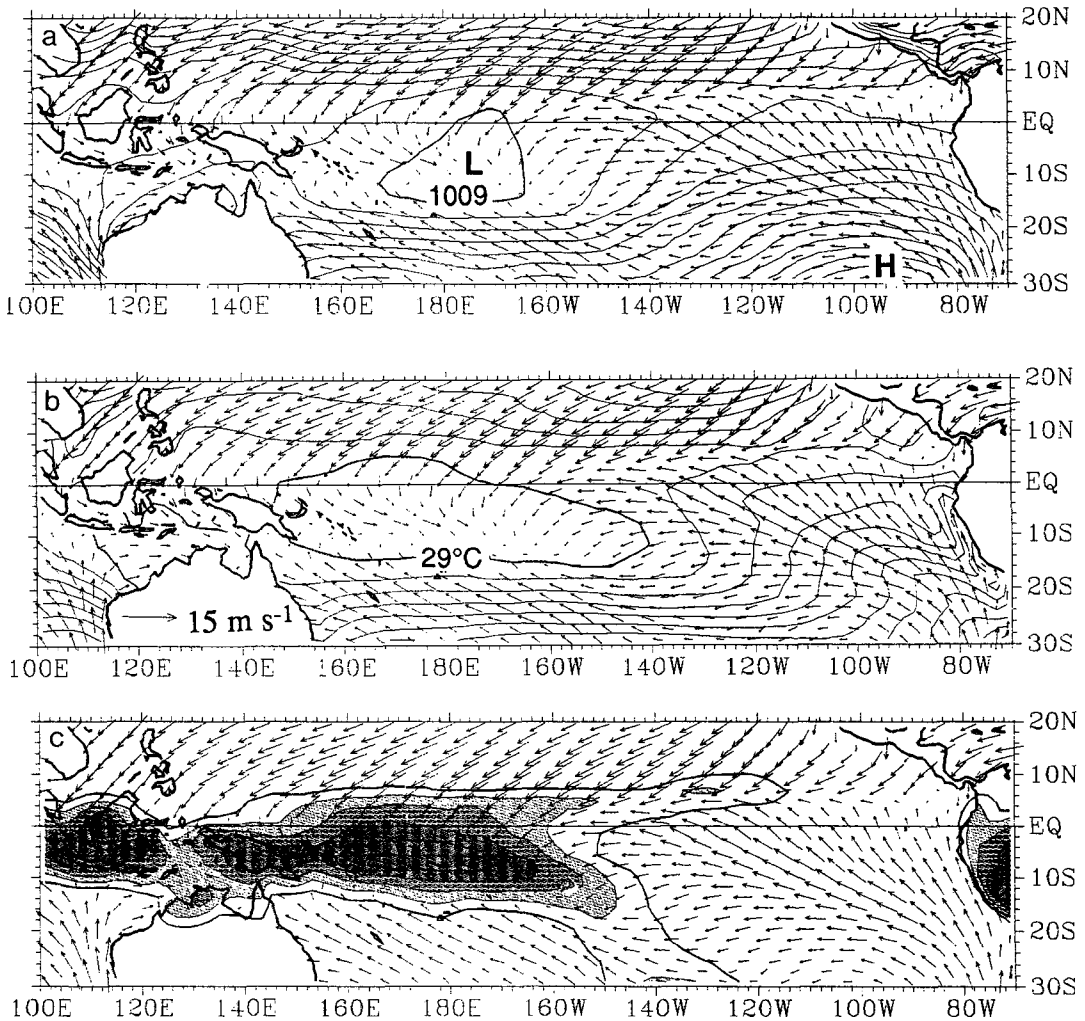

FIG. 11. December–February total (a) sea level pressure (mb) and surface wind, (b) SST (°C) and surface wind, and (c) OLR (W m^{-2}) and surface wind for a typical warm episode in the eastern equatorial Pacific. Plotting convention as in Fig. 8.

amount over the equatorial eastern Pacific during the cold seasons of warm and cold years. These parameters, together with surface wind speed, determine the energy balance at the sea surface.

a. Sea–air temperature difference

A crude measure of atmospheric boundary layer stability is the difference between surface[3] air temperature and SST: air temperatures at least 0.1°C cooler than the underlying SSTs are indicative of unstable conditions.[4] The virtual temperature effect slightly reduces the static stability because the air adjacent to the sea surface is saturated while the air 10 m above the ocean surface is not. For conditions over the equatorial cold tongue, air temperatures must exceed SSTs by at least 0.25°C for conditions to be stable, taking into account the adiabatic cooling of the air parcel as it rises 10 m. Figure 12 (upper panel) shows the sea–air temperature differences over the eastern tropical Pacific for the July–November cold episode composite. Negative sea–air temperature differences, indicative of a stable boundary layer, are observed over the cold, upwelling regions along the Peru coast and immediately to the south of the equator between 90°W and 140°W. Surface air temperatures exceed SSTs by about 0.5°C along the Peru coast and by a few tenths of a °C over the equatorial cold tongue. Large positive sea–air temperature differences (values > 1°C), indicative of unstable conditions, are observed along the ITCZ. The maximum sea–air temperature differences occur over the oceanic frontal zone east of 100°W, with values approaching 2°C. These large sea–air temperature differences over the oceanic frontal zone show that air parcels passing northward across the Equatorial Front have not had sufficient time to come into equilibrium with the underlying SST distribution.

The correlation pattern between the sea–air temperature differences over the eastern tropical Pacific and the equatorial SST index is shown in the lower panel of Fig. 12. Correlation coefficients > 0.4 in absolute value are indicated by shading; these are superimposed upon the cold composite SST and surface wind fields. Positive (negative) correlations are indicative of a tendency for more (less) unstable conditions during warm episodes than cold episodes. Negative correlations are observed in the unstable region over the oceanic frontal zone: the correlation coefficient between the SST index and air–sea temperature difference averaged over this shaded region is −0.81, with a corresponding regression coefficient of −0.3°C per °C of the SST index. This result is consistent with the fact that the frontal zone weakens during warm episodes, so the air flowing across the frontal zone should not be as cold relative to the underlying SST. There is also a small region of positive correlations over the equatorial cold tongue, where SST increases tend to weaken or eliminate the stable stratification. Presumably, the stable stratification that exists along the entire length of the coastal and equatorial upwelling zones should weaken during warm episodes; however, the signal is too weak[5] to detect with the available data.

b. Relative humidity

The near-surface moisture distribution over the tropical oceans is commonly represented by specific humidity [c.f., Weare et al. (1980) and Hastenrath and Lamb (1977)], a quantity which tends to be almost linearly related to the underlying SST field. Relative humidity, in contrast to specific humidity, is largely independent of SST and is thus a more informative indicator of the surface moisture field.

The distribution of relative humidity over the eastern tropical Pacific during the July–November cold episode composite is shown in Fig. 13 (upper panel). The most striking feature of the relative humidity distribution is the narrow band of high values that extends over the cold upwelling zones along the Peru coast and along 1°S in the eastern Pacific. Maximum values in these areas are ~87%: the highest relative humidities anywhere over the tropical oceans. The high values along the Peru coast are consistent with Prohaska (1973) who notes that at Lima, Peru (12°S on the coast) relative humidities of 80%–90% are typical in winter (June–October). These high values result from the strong low-level inversion that traps moisture in the surface layer (Prohaska 1973). A secondary maximum in relative humidity is observed along the ITCZ, where values approach 83%, and over the Gulf of Panama. The high relative humidities over the ITCZ and equatorial cold tongue are separated by a narrow band of low values (~80%) near 4°N in the eastern Pacific. The lowest relative humidities (<78%) are observed over the southeast Pacific in the main branch of the divergent southeast Trade Winds. The climatological mean relative humidity distribution over the eastern tropical Atlantic (not shown) is qualitatively similar to that over the eastern tropical Pacific. In the western Pacific, relative humidity is low (~77%) over the equatorial dry zone and slightly higher (~81%) over the warm pool and SPCZ.

The stability characteristics of the atmospheric surface layer may substantially influence the distributions of surface wind speed and relative humidity over the equatorial eastern Pacific. Over the cold tongue where

[3] Nominally 10 m.

[4] Adiabatic expansion will cool an air parcel lifted from the sea surface to a height of 10 m by 0.1°C.

[5] Sea–air temperature difference regression coefficients over the equatorial cold tongue are less than 0.1°C per °C of the SST index in absolute value.

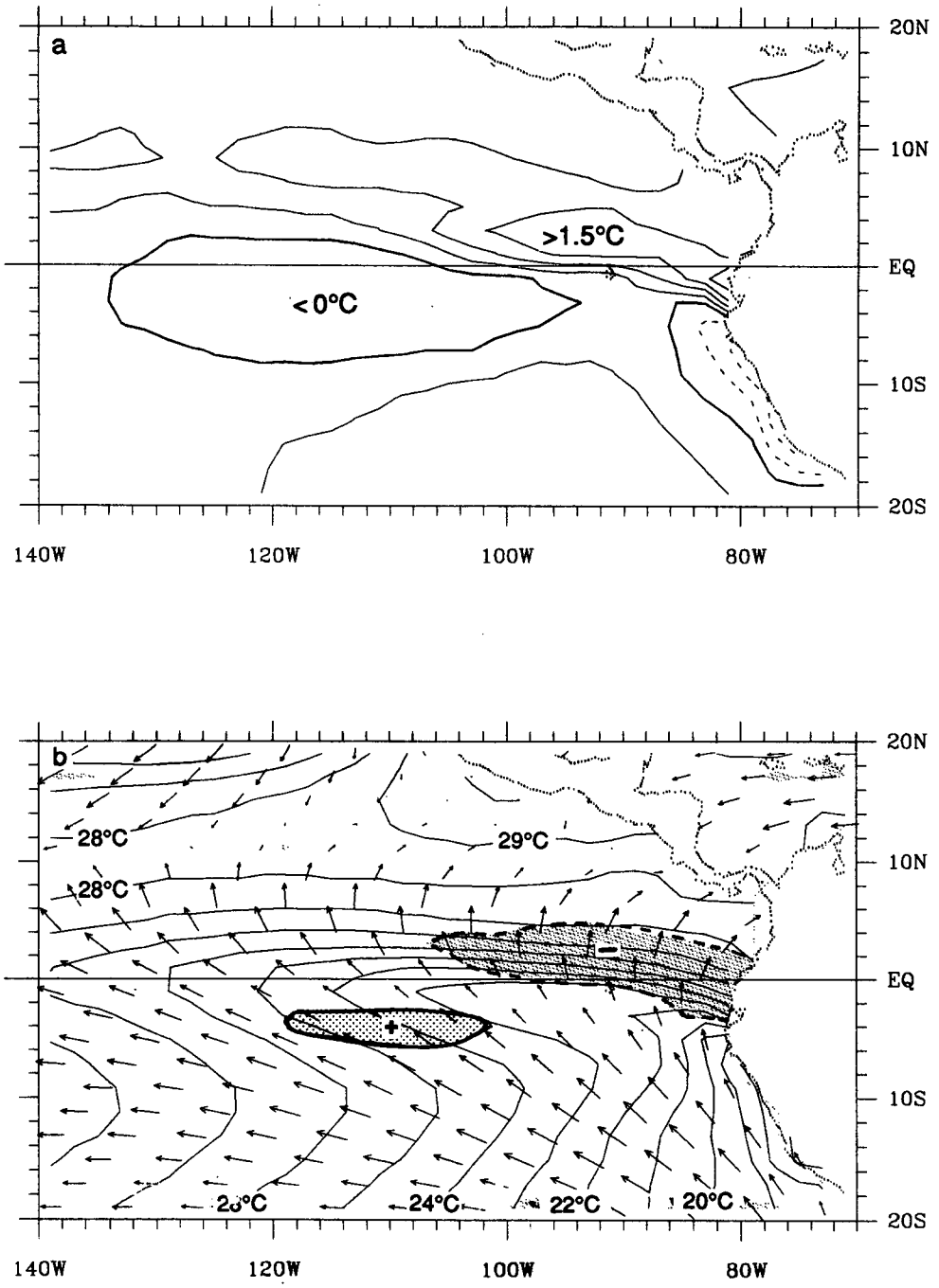

FIG. 12. (a) July–November sea–air temperature difference composite for a typical cold episode in the eastern equatorial Pacific. Contour interval = 0.5°C. The 0°C contour is darkened and negative contours are dashed. (b) Correlation coefficients > 0.4 in absolute value between July–November sea–air temperature differences and the equatorial SST index (shading), superimposed upon the cold composite SST and surface wind fields. The region of positive (negative) correlation coefficients is marked with a + (−) sign.

the stratification is stable, vertical mixing of moisture and momentum are inhibited within the atmospheric boundary layer, giving rise to light surface winds and high relative humidities; whereas over the northern edge of the oceanic frontal zone, where the stratification is highly unstable, vertical mixing is promoted and relatively dry, high momentum air is brought down to the surface. This interpretation needs to be verified with vertical profiles of wind and moisture in the planetary boundary layer.

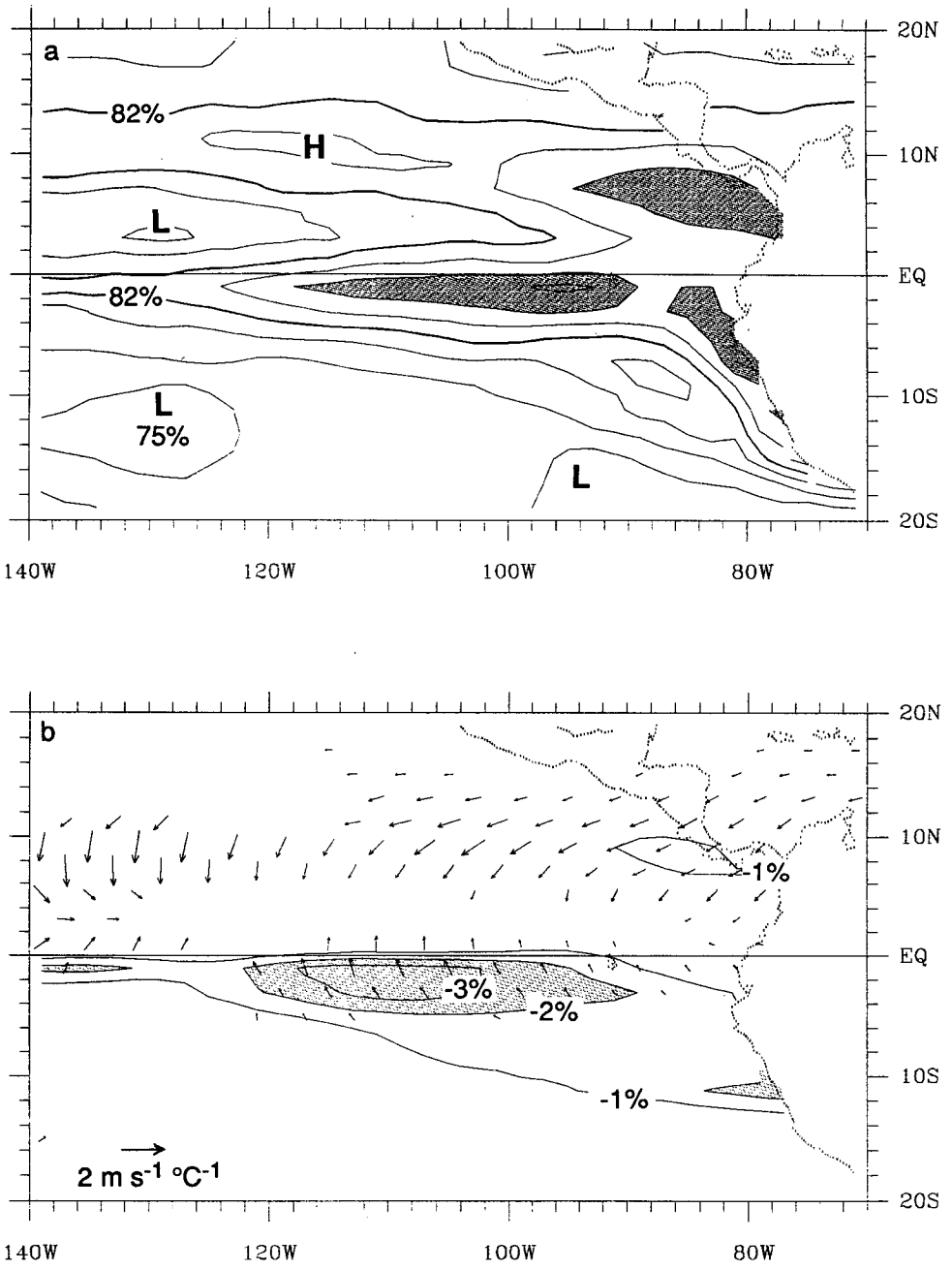

FIG. 13. (a) July–November relative humidity composite for a typical cold episode in the eastern equatorial Pacific. Contour interval = 2%. The 82% contour is darkened and values > 86% are shaded. (b) Regression coefficients of July–November relative humidity and surface wind upon the equatorial SST index. Contour interval = 1% per °C of the SST index; values < −2% °C^{-1} are shaded.

Regression coefficients of July–November relative humidity on the equatorial SST index are shown in the lower panel of Fig. 13, together with the corresponding surface wind regressions. Negative regression coefficients are observed over the region of the SST warming (compare with Fig. 5b), with values in excess of ~ −3% per °C of the SST index directly over the cold tongue. The decrease in relative humidity over the cold tongue during warm episodes is associated with southerly wind anomalies, which are indicative of an increase in surface wind speed.

The correlation coefficients between July–November

relative humidity, SST, and surface wind speed over the eastern Pacific cold tongue are summarized in Table 4. All three parameters are strongly correlated with one another ($|r| = 0.8$). One interpretation of these strong correlations is that the SST increases over the cold tongue destabilize the atmospheric surface layer, thereby effecting a redistribution of momentum and moisture within the lower part of the atmospheric planetary boundary layer. We note that the average July–November sea–air temperature difference over the cold tongue region [0°–4°S, 90°–120°W] is ~ -0.3°C (slightly stable) during cold years and $\sim$ zero (slightly unstable) during warm years. A similar phenomenon of boundary layer destabilization during warm episodes is observed at the coast of Peru (Enfield 1981).

c. *Cloudiness*

Figure 14 (upper panel) shows the distribution of cloud amount in oktas over the eastern tropical Pacific during the July–November cold composite. OLR values < 250 W m^{-2} are superimposed with shading to indicate regions of deep convection. A broad region of cloud amounts exceeding 6 oktas is observed between the equator and 9°N east of 110°W; this zone narrows to a thin band centered ~9°N farther to the west. The coasts of Ecuador and Peru experience the highest cloud amounts (>7 oktas). Cloudiness is slightly suppressed over the cold tongue between 90° and 120°W (where, it may be noted, relative humidity is a maximum!).

The band of maximum cloud cover is located distinctly to the south of the region of minimum OLR, particularly eastward of 110°W. The lack of a signature in the OLR field is because the clouds over the eastern Pacific are primarily stratus and stratocumulus decks with relatively warm cloud tops. The offset between minimum OLR and maximum cloudiness in the eastern equatorial Pacific is consistent with the results of Hastenrath and Lamb (1978) who compared the July–August climatological mean distributions of precipitation frequency and total cloudiness from ship observations. Sadler (1975) has also noted that "the mean monthly maximum cloud zone does not coincide with the tracks of migratory vortices" in this region. In addition, satellite measurements of reflectivity (cloud brightness) show enhanced reflectivity over the eastern Pacific south of the ITCZ (U.S. Dept. of Commerce and U.S. Air Force 1971).

TABLE 4. July–November correlation matrix for relative humidity (RH), SST, and surface meridional wind (v), each averaged over the region [0°–4°S, 90°–120°W], based on the period 1946–85.

	RH	SST	v
RH	1.00	−0.81	−0.79
SST		1.00	0.78
v			1.00

It seems plausible that the cloudiness maximum over the oceanic frontal zone between 90° and 110°W during July–November is a result of vigorous fluxes of latent and sensible heat implied by the large negative air–sea temperature differences and strong surface winds (see Fig. 12). According to this scenario, one would expect low-level clouds, such as stratocumulus, to be enhanced over the frontal zone relative to the cold tongue in analogy with the low-level convection that forms over the North Atlantic when cold continental air over the northeastern United States flows out over the warm waters of the Gulf Stream during winter. An alternative explanation for the cloudiness maximum, offered by Hastenrath and Lamb (1978), is that northeasterly winds aloft blow the tops of clouds formed in the ITCZ southward.

Warren et al. (1988) have compiled an atlas of climatological seasonal mean cloud types by 5° grid squares over the global oceans based on 30 years of ship observations. The cloud types are grouped into four categories: (1) stratus, stratocumulus, and fog, (2) altostratus and altocumulus, (3) cumulus and (4) cumulonimbus. Figure 15 shows meridional profiles of the four cloud groups during September–November averaged over the region from 90°W to 100°W. Overall cloud amount increases between 0°–5°S and 0–5°N, in accord with the COADS observations of total cloud amount. The increase is caused by both low and middle level clouds. From 0°–5°N to 5°–10°N, the fraction of sky covered by stratus, stratocumulus, and fog decreases substantially while the total cloud amount barely changes: low cloud types account for ~60% of the cloud cover at 0°–5°N but only ~30% at 5°–10°N.

Regression coefficients of July–November cloudiness and OLR (shaded) upon the equatorial SST index are shown in the lower panel of Fig. 14. The two fields exhibit contrasting features. Negative cloud regression coefficients, indicative of a decrease in total cloud cover during warm episodes, are observed in the region between Ecuador and the Galapagos Islands and to the immediate north of the equatorial cold tongue; while negative OLR regression coefficients, indicative of enhanced deep convection during warm episodes, occur farther north, ~6°N. The correlation coefficient between cloud amount averaged over the region [6°N–6°S, 120°–70°W] and the equatorial SST index is −0.84 based on July–November averages during the period 1951–85 (there were too few observations in the years 1946–50 for cloud cover estimates to be reliable). Hence, the tendency for reduced cloud cover over the equatorial eastern Pacific during warm episodes is rather robust. Enfield (1981) notes that winters at Lima, Peru (12°S on the coast) are unusually sunny during warm episodes, consistent with our results.

The decreased cloud cover immediately to the north of the cold tongue during warm episodes may be a consequence of diminished sea-to-air energy fluxes due to reduced sea–air temperature differences. However,

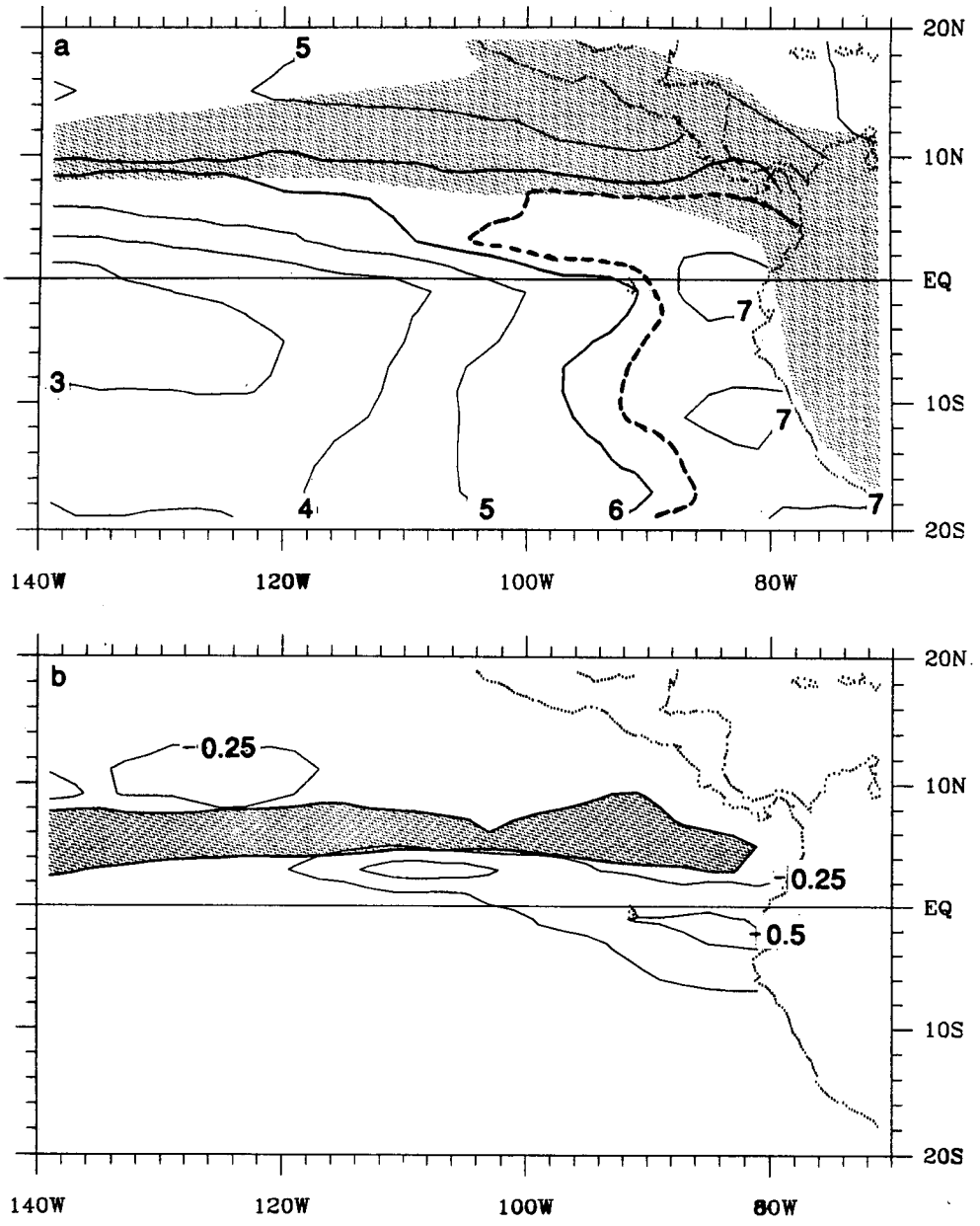

FIG. 14. (a) July–November cloud amount in oktas for a typical cold episode in the eastern equatorial Pacific. The dashed line is the 6.5 okta contour. Shading denotes OLR values < 250 W m^{-2}. (b) Regression coefficients of July–November cloud amount (oktas per °C of the SST index) upon the equatorial SST index. Shading denotes OLR regression coefficients < -10 W m^{-2} °C^{-1}.

we note that cloud cover is not as strongly correlated with sea–air temperature difference as with SST in this region. Furthermore, this mechanism does not explain the decrease in cloud cover over the tongue of cold water extending westward from the northern Peru coast, where air–sea temperature differences are indicative of *less* stable conditions during warm episodes. Enfield (1981) has suggested that the dissipation of the stratiform cloud deck at Lima, Peru (12°S) during warm episodes is due to the mixing of moist air in the cloud layer with drier air above it; a process that is promoted by the destabilization of the air column.

6. Discussion

The large-scale circulation changes in the tropical Pacific during basin-wide warm episodes may be summarized in terms of the movements of the major convective zones as documented in Fig. 16. The ITCZ expands southward toward the positive SST anomalies

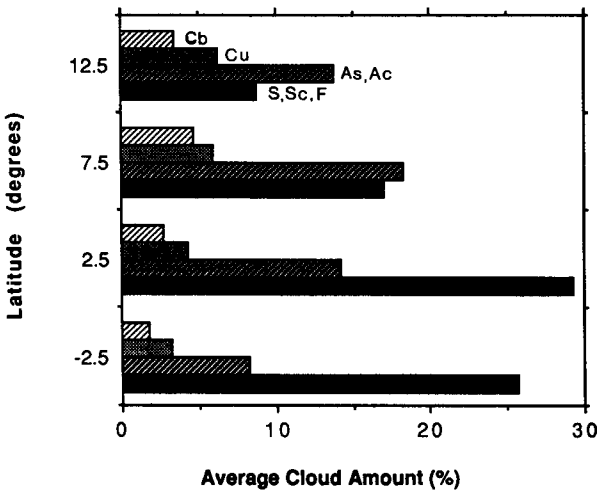

FIG. 15. Meridional profiles of climatological mean September–November cloud amount (%), stratified by cloud type, for the longitude band 90°–100°W. Cloud type categories are: Cb = Cumulonimbus, Cu = Cumulus, As = Altostratus, Ac = Altocumulus, S = Stratus, Sc = Stratocumulus, and F = Fog. Values from Warren et al. (1988).

along the equator and the convection over Indonesia shifts eastward toward the anomalous warming in the central and eastern Pacific. Both convective zones follow the warmest sea surface temperatures and intensify, as evidenced by the net decrease in OLR over the Indonesia–Pacific sector during warm episodes. Both regions of anomalous convection are characterized by anomalous confluence in the meridional component of the surface wind field, consistent with Wang (1987). The correspondence between the negative OLR and surface wind convergence anomalies during warm episodes support the conclusions of RC, Cornejo-Garrido and Stone (1977), and Ramage and Hori (1981) that "large-scale vapor flux convergence rather than enhanced local evaporation is the main source of water vapor for the enhanced precipitation" (RC, p. 379). The wind anomalies over the tropical western Pacific differ substantially from Gill's (1980) model of the response of the tropical atmospheric circulation to latent heat release in deep convection. In Gill's formulation the region of anomalous convection is characterized by diffluent meridional wind anomalies and confluent zonal wind anomalies in the low-level flow, whereas in the surface observations the meridional wind anomalies are confluent and the maximum westerly wind anomaly is centered over the anomalous convection.

In the climatological mean, surface wind convergence is a factor of two to three larger into the eastern Pacific ITCZ than into the convective region over Indonesia, yet rainfall amounts in the two areas are not appreciably different (see Deser 1989). Since specific humidity differs by only 10%–15% between the two regions, and evaporation from the sea surface is weak in both regions due to the light winds and high relative humidities, this apparent discrepancy suggests that the moisture convergence extends through a deeper layer in the west than in the east. Assuming an average rainfall rate of 20 cm/month and a specific humidity of 18 g/kg, the depth of the convergence in the eastern Pacific ITCZ would have to be ~60 mb where typical surface convergences are $\sim 7 \times 10^{-6}$ s^{-1}, and it would have to be ~200 mb in the western equatorial Pacific where typical surface convergences are only $\sim 2 \times 10^{-6}$ s^{-1}. Moisture budget studies of tropical easterly waves in the western Pacific and eastern Atlantic support this conclusion: over the western equatorial Pacific, moisture convergence in the waves extends between the surface and ~750 mb [Nitta (1970), Reed and Recker (1971), and Wallace (1971)] while over the equatorial eastern Atlantic (which is presumably similar to the eastern Pacific) the moisture convergence is much shallower and stronger [Thompson et al. (1979) and Houze and Betts (1981)]. [Convection associated with the westward propagating synoptic-scale waves provides much of the precipitation in these areas.] In view of these differences in the climatology, it is perhaps not surprising that the ratio of *anomalous* OLR to *anomalous* surface wind convergence during warm episodes is a factor of two to three larger over the western than the eastern tropical Pacific (see Table 2). This observational finding is supported by the modeling experiments of Mechoso et al. (1987) who examined the response of the atmospheric circulation to SST anomalies in the eastern equatorial Pacific using a general circulation model with detailed parameterizations of planetary boundary layer and moist convective processes. They found that the model's anomalous moisture convergence is confined to the planetary boundary layer in the eastern Pacific but extends into the free atmosphere (and is, in fact, larger there than in the boundary layer) over the western Pacific. The idea that the anomalous moisture convergence may extend above the planetary boundary layer in the western Pacific is further supported by the fact that westerly wind anomalies at islands in the equatorial western Pacific are larger at 850 mb than at the surface during warm episodes (Harrison and Gutzler 1986; Deser 1989).

As noted above, convection in the ITCZ is observed to be more intense (as evidenced by the lower OLR) during warm episodes than during cold episodes, consistent with the findings of Liebmann and Hartmann (1982). Is this intensification accompanied by an increase in surface wind convergence? Meridional profiles of surface wind divergence and OLR in the eastern Pacific (Fig. 17) show that there is no appreciable difference in meridionally integrated surface convergence (upper panel) north of the equator (the convergence zone is stronger but narrower during the cold years); yet the OLR profiles (lower panel) show a substantial difference in convective cloudiness at latitudes between

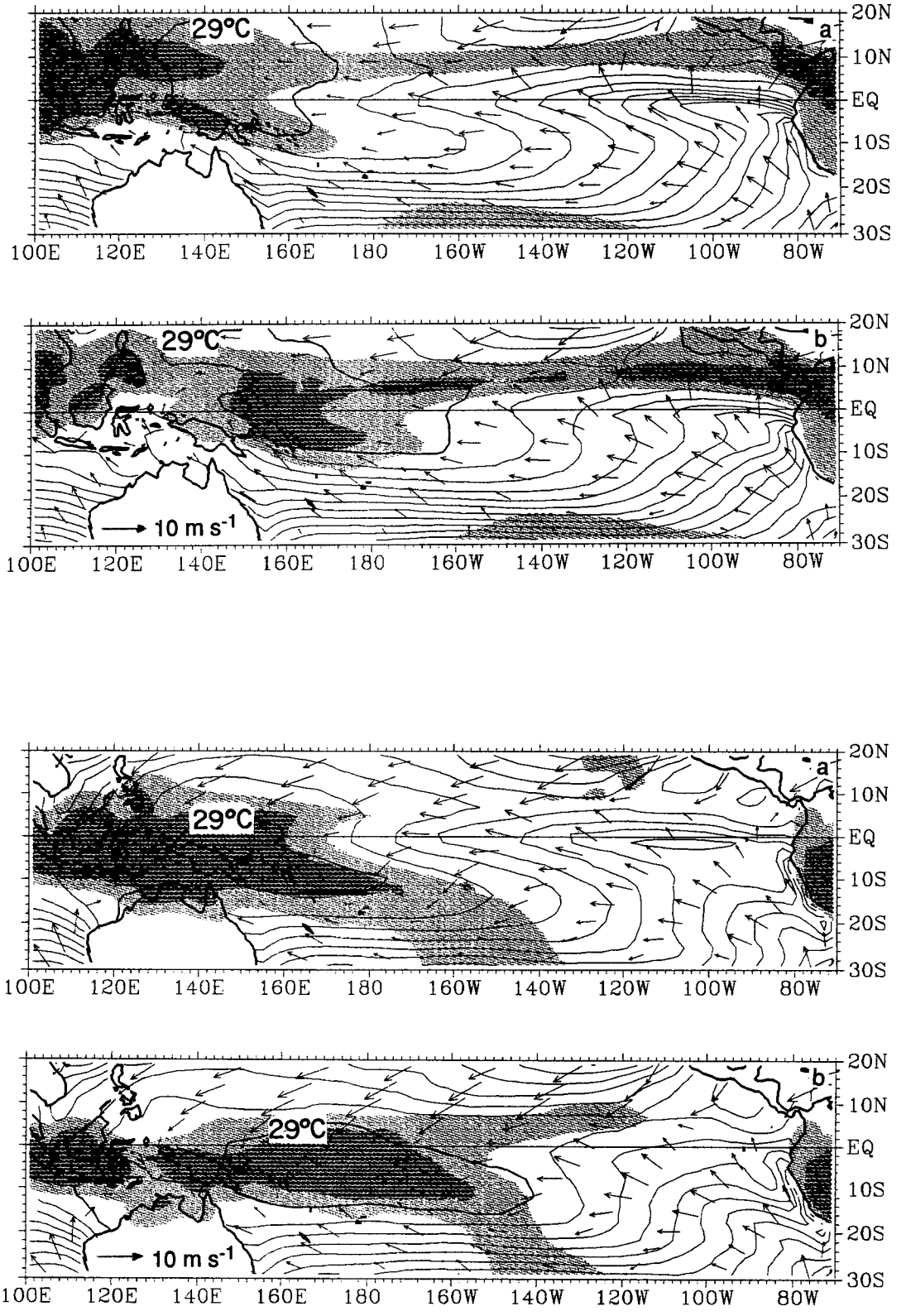

FIG. 16. Total SST, OLR and surface wind distributions for (a) cold episodes and (b) warm episodes. Upper two panels describe conditions during July–November; lower two panels describe conditions during December–February. Contour interval = 1°C; the 29°C contour is darkened. Light (dark) shading denotes OLR values < 240 (<220) W m^{-2}.

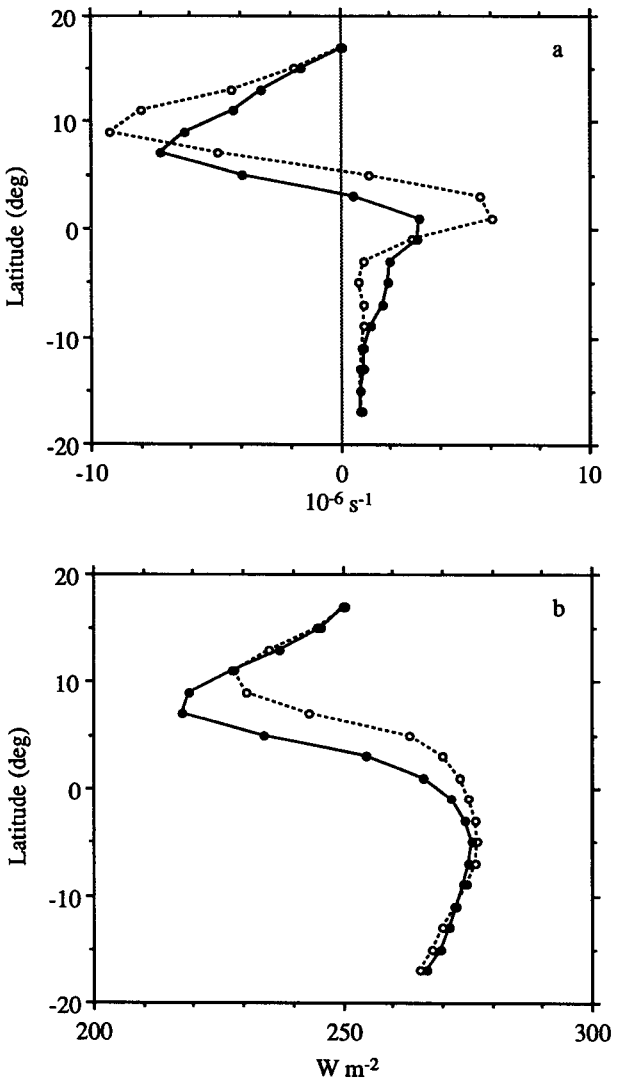

FIG. 17. Meridional profiles of July–November (a) surface wind divergence (10^{-6} s^{-1}) and (b) OLR (W m^{-2}), averaged over the region 90°–150°W during cold and warm episodes. Dashed (solid) lines denote profiles for cold (warm) episodes.

the equator and 10°N. Similar differences are observed for the March–May season (not shown). It is unlikely that the increase in surface moisture (~1 g/kg^{-1}, a fractional increase of ~5–10%) can fully account for the enhanced convection in the ITCZ during warm episodes. It follows that the moisture convergence must extend through a deeper layer during the warm years than the cold years. We note that the net lowering of sea level pressure in the equatorial trough relative to the subtropical highs in the eastern Pacific is consistent with the notion that the mass circulation associated with the ITCZ is intensified during warm episodes.

The center of below normal sea level pressure along the equator in the eastern Pacific coincides with the largest positive SST anomalies during basin-wide warm episodes. Pressure and SST in the equatorial eastern Pacific during the cold season are strongly negatively correlated ($r = -0.9$): the corresponding regression coefficient is −0.65 mb/°C. Lindzen and Nigam (1987) have postulated that the sea level pressure distribution over the tropical oceans is a hydrostatic reflection of the baroclinity in the planetary boundary layer induced by the underlying SST gradients. According to their hypothesis, a 1°C SST anomaly would become mixed by turbulent processes through the depth of the atmospheric boundary layer (about 1.5 km), resulting in a sea level pressure decrease of about 0.7 mb[6]. The observed regression coefficient between pressure and SST in the eastern equatorial Pacific is in good agreement with this simple model. Rawinsonde data (50 mb vertical resolution) for Guayaquil (3°S) on the Ecuador coast confirm that the July–November temperature anomalies in a warm year (1957) relative to a cold year (1960) are confined to the lowest 150 mb (Deser 1989). We are unable to verify this finding for other warm years since our Guayaquil record is limited to the period 1957–60. Similar results are obtained for Canton Is. (3°S, 172°W), near the western edge of the region of positive SST anomalies (Deser 1989).

Although the Lindzen and Nigam (1987) model appears to account for at least part of the pressure change in the equatorial eastern Pacific, there is no simple proportionality between the pressure and SST regression coefficients over the entire tropical Pacific domain (see Fig. 5). In particular, the pressure regressions in the equatorial western Pacific are disproportionately large with respect to the local SST regressions (e.g., temperature anomalies as large as the observed SST anomalies would have to extend through a layer at least 500 mb deep, well above the boundary layer, in order to account for the surface pressure anomalies). In addition, pressure and SST are only weakly correlated over the western equatorial Pacific where the anomalies in both fields are small.

The results on sea–air temperature difference, relative humidity, and cloudiness presented in section 5 have implications for the surface energy balance. In particular, they suggest the existence of a negative feedback between the surface energy fluxes and the strength of the Equatorial Front. In a cold year, sea-to-air fluxes of latent and sensible heat over the cold tongue are strongly suppressed because of the light winds, negative sea–air temperature differences, and high relative humidities; while large positive sea–air temperature differences, low relative humidities, and strong surface winds over the northern half of the frontal zone induce vigorous fluxes of sensible and latent heat that act to cool the oceanic mixed layer. These

[6] The "back-pressure effect" in Lindzen and Nigam's (1987) model may be expected to somewhat reduce the response in the sea level pressure field.

contrasting fluxes tend to weaken the SST difference across the frontal zone. The large sensible and latent heat fluxes on the north side of the zone may also favor the development of low clouds, which should further weaken the frontal zone by decreasing the incident solar radiation over the front relative to that over the cold tongue. These effects should be substantially reduced during warm episodes, when sea-to-air fluxes are enhanced over the cold tongue because of the lower relative humidities and stronger winds, while they are reduced over the frontal zone, because of the weaker winds and lower cloud amounts. From the point of view of the oceanic mixed layer, the meridional gradient in the fluxes produces a southward (down-gradient) heat flux across the Equatorial Front, which increases in proportion to the strength of the front. In this sense, the surface heat fluxes play a role in the oceanic heat balance analogous to the tropical instability waves in the ocean (Philander et al. 1986). Deser (1989) estimates that the surface energy fluxes would reduce the strength of the frontal zone by a factor of $1/e$ in 1–2 months if no other processes were acting to maintain it; this damping time is found to be approximately the same for both warm and cold years.

Acknowledgments. We thank the reviewers for their helpful comments on an earlier version of the manuscript. We are indebted to Todd P. Mitchell for sharing his unpublished work on the correlations between sea level pressure and SST in the equatorial eastern Pacific. We thank Kay Dewar for her assistance in preparing the figures. This work was supported by the Climate Dynamics Program of the National Science Foundation under grant ATM-8318853.

REFERENCES

Barnett, T. P., 1985: Variations in near-global sea level pressure. *J. Atmos. Sci.*, **42,** 478–501.

Climate Diagnostics Bulletins, 1988: U.S. Dept. of Commerce, NOAA/NWS/NMC. V. E. Kousky, Ed., Climate Analysis Center, Washington DC.

Cornejo-Garrido, A. G., and P. H. Stone, 1977: On the heat balance of the Walker Circulation. *J. Atmos. Sci.*, **34,** 1155–1162.

Deser, C., 1989: Meteorological Characteristics of the El Niño/Southern Oscillation Phenomenon. Ph.D. thesis, University of Washington, 195 pp.

Deser, C., and J. M. Wallace, 1987: El Niño events and their relationship to the Southern Oscillation: 1925–86. *J. Geophys. Res.*, **92,** 14 189–14 196.

Doberitz, R., 1968: Cross spectrum analysis of rainfall and sea temperature at the equatorial Pacific Ocean—A contribution to the El Niño phenomenon. *Bonner Meteor. Abhand.*, **7,** 3–53.

Enfield, D. B., 1981: Thermally driven variability in the planetary boundary layer above Lima, Peru. *J. Geophys. Res.*, **86,** 2005–2016.

Fletcher, J. O., R. J. Slutz and S. D. Woodruff, 1983: Towards a comprehensive ocean-atmosphere data set. *Trop. Ocean-Atmos. Newslett.*, **20,** 13–14.

Gill, A. E., 1980: Some simple solutions for heat-induced tropical circulation. *Quart. J. Roy. Meteor. Soc.*, **106,** 447–462.

Gruber, A., 1972: Fluctuations in the position of the ITCZ in the Atlantic and Pacific Oceans. *J. Atmos. Sci.*, **29,** 193–197.

Harrison, D. E., 1987: Monthly mean island surface winds in the central tropical Pacific and El Niño events. *Mon. Wea. Rev.*, **115,** 3133–3145.

——, and D. S. Gutzler, 1986: Variability of monthly-averaged surface and 850 mb winds at tropical Pacific islands. *Mon. Wea. Rev.*, **114,** 285–294.

Hastenrath, S., and P. J. Lamb, 1977: *Climatic Atlas of the Tropical Atlantic and Eastern Pacific Oceans.* The University of Wisconsin Press, 113 pp.

Houze, R. A., Jr., and A. K. Betts, 1981: Convection in GATE. *Rev. Geophys. Space Phys.*, **19,** 541–576.

Kiladis, G. N., and H. van Loon, 1988: The Southern Oscillation. Part VII: Meteorological anomalies over the Indian and Pacific sectors associated with the extremes of the oscillation. *Mon. Wea. Rev.*, **116,** 120–136.

Liebmann, B., and D. L. Hartmann, 1982: Interannual variations of outgoing IR associated with tropical circulation changes during 1974–78. *J. Atmos. Sci.*, **39,** 1153–1162.

Lindzen, R. S., and S. Nigam, 1987: On the role of sea surface temperature gradients in forcing low-level winds and convergence in the tropics. *J. Atmos. Sci.*, **44,** 2440–2458.

Mechoso, C. R., A. Kitoh, S. Moorthi and A. Arakawa, 1987: Numerical simulations of the atmospheric response to a sea surface temperature anomaly over the equatorial eastern Pacific Ocean. *Mon. Wea. Rev.*, **115,** 2936–2956.

Meehl, G. A., 1987: The annual cycle and interannual variability in the tropical Pacific and Indian Ocean regions. *Mon. Wea. Rev.*, **115,** 27–50.

Nitta, T., 1970: Statistical study of tropospheric wave disturbances in the tropical Pacific region. *J. Meteorol. Soc. Jpn.*, **48,** 47–60.

Pazan, S. E., and G. Meyers, 1982: Interannual fluctuations of the tropical Pacific wind field and the Southern Oscillation. *Mon. Wea. Rev.*, **110,** 587–600.

Philander, S. G. H., 1985: El Niño and La Niña. *J. Atmos. Sci.*, **42,** 2652–2662.

——, and R. C. Pacanowski, 1981: The oceanic response to cross-equatorial winds (with application to coastal upwelling in low latitudes). *Tellus,* **33,** 201–210.

——, W. J. Hurlin and R. C. Pacanowski, 1986: Properties of long equatorial waves in models of the seasonal cycle in the tropical Atlantic and Pacific Oceans. *J. Geophys. Res.*, **91**(C12), 14 207–14 211.

Prohaska, F. J., 1973: New evidence on the climatic controls along the Peruvian coast. *Coastal Deserts: Their Natural and Human Environments.* D. Anadon, A. Wilson, Eds., University of Arizona Press, 207 pp.

Quinn, W. H., V. T. Neal and S. E. Antunez de Mayolo, 1987: El Niño occurrences over the past four and a half centuries. *J. Geophys. Res.*, **92,** 14 449–14 461.

Ramage, C. S., and A. M. Hori, 1981: Meteorological aspects of El Niño. *Mon. Wea. Rev.*, **109,** 1827–1835.

Rasmusson, E. M., and T. H. Carpenter, 1982: Variations in tropical sea surface temperature and surface wind fields associated with the Southern Oscillation/El Niño. *Mon. Wea. Rev.*, **110,** 354–384.

Reed, R. J., and E. E. Recker, 1971: Structure and properties of synoptic-scale wave disturbances in the equatorial western Pacific. *J. Atmos. Sci.*, **28,** 1117–1133.

Sadler, J. C., 1975: Upper Tropospheric Circulation over the Global Tropics. Dept. of Meteorology, University of Hawaii, UHMET 75-05, 25 pp.

——, M. A. Lander, A. M. Hori and L. K. Oda, 1987: *Tropical Marine Climatic Atlas, Vol. 2., Pacific Ocean.* UHMET 87-02, University of Hawaii, 15 pp.

Taylor, R. C., 1973: An atlas of Pacific island rainfall. *Hawaii Inst. Geophys.* Data Rep. No. 25, HIG-73-9, 175 pp. [NTIS No. AD767073].

Thompson, R. M., S. W. Payne, E. E. Recker and R. J. Reed, 1979: Structure and properties of synoptic-scale wave disturbances in the intertropical convergence zone of the eastern Atlantic. *J. Atmos. Sci.*, **36,** 53–72.

Trenberth, K. E., 1976: Spatial and temporal variations of the Southern Oscillation. *Quart. J. Roy. Meteor. Soc.*, **102,** 639–653.

Troup, A. J., 1965: The "Southern Oscillation." *Quart. J. Roy. Meteor. Soc.*, **91,** 490–506.

U.S. Department of Commerce and U.S. Air Force, 1971: Global atlas of relative cloud cover: 1967–1970 based on data from meteorological satellites. NOAA National Environmental Satellite Service/USAF (Air Weather Service) Environmental Technical Applications Center Tech. Rep., 237 pp.

Wallace, J. M., 1971: Spectral studies of tropospheric wave disturbances in the tropical western Pacific. *Rev. Geophys.*, **9,** 557–612.

——, T. P. Mitchell and C. Deser, 1989: The influence of sea surface temperature upon surface wind in the eastern equatorial Pacific: Seasonal and interannual variability. *J. Climate,* **2,** 1492–1499.

Wang, S. W., 1987: A version of the circulation scheme in the equatorial zone. *Beitr. Phys. Atmos.*, **60,** 478–487.

Warren, S. G., C. J. Hahn, J. London, R. M. Chervin and R. L. Jenne, 1988: Global distribution of total cloud cover and cloud type amounts over the ocean. NCAR Tech. Note, *TN-317+STR.*

Weare, B. C., A. R. Navato and R. E. Newell, 1976: Empirical orthogonal analysis of Pacific sea-surface temperatures. *J. Phys. Oceanogr.*, **6,** 671–678.

——, P. T. Strub and M. D. Samuel, 1980: Marine climatic atlas of the tropical Pacific Ocean. Contributions in Atmospheric Science No. 20., Department of Land, Air and Water Resources, University of California, Davis.

Wright, P. B., 1977: The Southern Oscillation—Patterns and mechanisms of the teleconnections and the persistence. *Hawaii Insti. Geophys.* Rep. HIG-77-13, Honolulu, 107 pp.

——, T. P. Mitchell and J. M. Wallace, 1985: Relationships between surface observations over the global oceans and the Southern Oscillation. NOAA Data Rep. ERL PMEL-12, 61 pp.

——, J. M. Wallace, T. P. Mitchell and C. Deser, 1988: Correlation structure of the El Niño/Southern Oscillation phenomenon. *J. Climate,* **1,** 609–625.

Wyrtki, K., 1975: El Niño—the dynamic response of the equatorial Pacific Ocean to atmospheric forcing. *J. Phys. Oceanogr.*, **5,** 572–584.

Zebiak, S. E., and M. A. Cane, 1987: A model El Niño/Southern Oscillation. *Mon. Wea. Rev.*, **115,** 2262–2278.